Source Localization with Feedback Beamforming

Itay Yehezkel Karo

Source Localization with Feedback Beamforming

Research Thesis

Submitted in partial fulfillment of the requirements
for the degree of Master of Science in Electrical Engineering

Itay Yehezkel Karo

Submitted to the Senate
of the Technion — Israel Institute of Technology
Tamuz 5781 Haifa June 2021

This research was carried out under the supervision of Prof. Israel Cohen, in the Faculty of Electrical and Computer Engineering and Dr. Tsvi G. Dvorkind from RAFAEL.

List of publications

Itay Yehezkel Karo, Tsvi Gregory Dvorkind, and Israel Cohen. Source localization with feedback beamforming. *IEEE Transactions on Signal Processing*, 69:631–640, 2021.

Acknowledgements

First, I would like to thank my wife, Hadas, for giving me time, space and endless encouragement to finish this work inspite of all the Covid-19 realted difficulties and quarantines. Also great gratitude is to my parents, who encouraged and helped me to set high goals and achieve them.

I would also like to thank Dr. Tsvi Dvorkind for guiding me to ask the right questions without missing any details, which proved itself worthwhile with the paper being almost accepted with the first submission.

Special thanks goes to Prof. Israel Cohen for giving great guidance and crucial insights in addition to sharing his vast knowledge and experience.

The generous financial help of the Technion is gratefully acknowledged.

Contents

List of Figures

Abstract

The general field of array processing has been thoroughly studied throughout several decades. The array sensors' spatial diversity enables the extraction of spatial information about impinging signals, thus laying the ground for wide range of applications. The array size and the number of its elements have significant influence on the achievable array performance, such as signal to noise ratio (SNR) improvement, spatial separation capabilities, directivity, array gain, source localization, etc.

Localization applications are divided to several groups, each featuring a different approach for estimating the spatial parameters of objects in the arena. The most basic approach is *beamforming*, where the arena (or a part of it) is continuously scanned by steering (mechanically or electronically) the array to all possible directions in search for objects. Another approach, more commonly used, is subspace-based processing which exploits the orthogonality between the array manifold (i.e. the array's excitations set of impinging planewaves from all directions) and the noise subspace. In this scheme the input signal is projected onto the array manifold - thus mitigating non directional noise interference. Statistical processing, although costly in terms of computation effort, is also in use. One important example is the maximum-likelihood (ML) approach which assumes a known probability density function (PDF) for the input signal or the noise.

In this work we revisit the *beamforming* approach. Inspired by the analogy between spatial processing with uniform linear array (ULA) and temporal finite impulse response (FIR) filtering, we search for the spatial counterpart of the temporal infinite impulse response (IIR) filter. To this end, we formulate a localization problem and suggest a feedback based approach, featuring low complexity and high spatial performance in the mere excess of integrating a transmitter to the array. Considering RADAR-like arrays, the transmitter is already in place, hence a mere processing modification suffices.

Assuming the target of interest has a mirror-like behaviour (i.e., reflects its impinging signals), the spatial feedback between the array and the target is created by continuously retransmitting a synthesized version of the impinging signal (and its reflections) to the target. In this manner, a spatial loop is created, which is shown to be equivalent of enlarging the array's aperture in terms of spatial resolution.

Using a traditional beamforming performance analysis, the beamwidth, peak to side-lobe ratio, array directivity and white noise sensitivity are evaluated for the feedback based array. A significant improvement in all aspects is shown, while thoroughly discussing the conditions for

enhanced performance. Considering ideal scenarios, the feedback beamformer (FB) virtually achieves an infinite aperture, increasing the available spatial information about the target and significantly improves the array's spatial performance.

Taking into account the unavoidable estimation errors and uncertainties, we find that the basic feedback integrated beamformer is very sensitive to even mild range errors. As a solution, we propose a more complex architecture, using two harmonics, which we call *dual-frequency feedback beamformer*. We also thoroughly analyse the proposed solution and find that it features low and controllable estimation errors sensitivity in the mere expense of doubling the computation effort.

Acronyms

CB Conventional beamformer.

CRLB cramér Rao lower bound.

DF dual frequency.

DOA direction of arrival.

FB feedback beamformer.

FIM fisher information matrix.

FIR finite impulse response.

HOS high order statistics.

HPBW half power beamwidth.

ICA independent components analysis.

IIR infinite impulse response.

MUSIC multiple signal classification.

MVDR minimum Variance Distortionless Response.

PCA principal component analysis.

PDF probability density function.

RADAR Radio Detection And Ranging.

RHS right hand side.

SF single frequency.

SNR signal to noise ratio.

ULA uniform linear array.

UWB ultra wide band.

Notations

$A_{i,j}$ The i, j-th element of matrix $\boldsymbol{A}$.

B beampattern.

R Distance to target.

$Z(\omega)$ Array's frequency-domain output.

λ Wavelength.

$\mathcal{D}$ Directivity.

$\mathcal{H}$ Normalized beampattern.

ω Radial frequency.

θ Electrical phase.

θ_d Geometrical angle.

$\boldsymbol{A}$ A Matrix.

$\boldsymbol{A}^*$ Conjugate of matrix $\boldsymbol{A}$.

$\boldsymbol{A}^H$ Hermitian (conjugated) transpose of matrix $\boldsymbol{A}$.

$\boldsymbol{A}^T$ Transpose of matrix $\boldsymbol{A}$.

$\boldsymbol{v}$ A vector.

$\boldsymbol{v}^*$ Conjugate of vector $\boldsymbol{v}$.

$\boldsymbol{v}^H$ Hermitian (conjugated) transpose of vector $\boldsymbol{v}$.

$\boldsymbol{v}^T$ Transpose of vector $\boldsymbol{v}$.

c Wave's propagation velocity.

d Array's inter-element spacing.

v_i The i-th element of vector $\boldsymbol{v}$.

$z(t)$ Array's temporal output.

$\boldsymbol{d}$ Steering vector.

Chapter 1

Introduction

1.1 Background and Motivation

The general field of array processing has been thoroughly studied throughout several decades. The array sensors' spatial diversity enables the extraction of spatial information about impinging signals, thus laying the ground for wide range of applications, such as localizing a transmitting source [31, 15], blindly separating mixtures of impinging signals [8], improving SNR [37], and many more.

The ULA has always been a point of interest, due to its simplicity of analysis [35, 3]. The array size and the number of its elements (N) have significant influence on the obtained array performance, such as SNR improvement, spatial separation capabilities and its spatial response's degrees of freedom (DOF).

Early algorithms for direction of arrival (DOA) estimation were based on the beamforming concept [13], where the array's reception beam is steered (mechanically or electronically) to multiple directions in search of received energy peaks which are interpreted as valid emitters. One notable improvement to the conventional beamformer [35] was Capon's beamformer (aka minimum variance distortionless response (MVDR)) which attempts to minimize the power contributed by noise and any signals coming from other directions than the DOA of interest, while maintaining a fixed gain in the desired direction.

The most practically used approach in DOA estimators, referred as the subspace based estimation, involves invariant subspace analysis of observed covariance matrices. Early research includes PCA and errors-in-variables time series analysis [13]. However, the tremendous interest in the subspace approach is mainly due to the introduction of the MUSIC (Multiple SIgnal Classification) algorithm [27] which decomposes the estimated covariance matrix to its signal and noise eigenvectors, using orthogonal projection exploiting the fact that the noise subspace is orthogonal to the signal subspace. It is interesting to note that while earlier works were mostly derived in the context of time series analysis and only later applied to the sensor array problems, MUSIC was originally presented as a DOA estimator.

A less practical, but optimal in the sense of root mean square error (RMSE) [13], is the maximum likelihood (ML) approach which tries to find the most probable DOA assuming a

known PDF. Though this approach served as a basis for extensive research, leading to more advanced concepts such as the independent component analysis (ICA) [12], in the context of practical DOA estimation it's computational effort is high. Adding the fact that sub-optimal methods such as MUSIC were proven to achieve the Cramér Rao lower bound (CRLB) under some practical assumptions (e.g. non-coherent signals) [32], these sub optimal estimators are substantially more common in practice.

In pursuit of spatial performance improvement, namely higher spatial separation and selectivity of arriving signals, many approaches were suggested. One approach, commonly referenced as "virtual arrays" [22, 6, 9] deals with the extraction of samples originated in sensors that do not really exist, by using high (higher than 2) order statistics and manipulating multiple statistical cross-terms in order to estimate statistical characteristics of signals impinging in missing sensors.

Using a similar approach, the $2q$-MUSIC algorithm [7], enables the use of N^{2q} "virtual elements", by calculating the q'th order statistics. Another approach, involving different array geometries, examined minimum redundancy arrays [19, 24, 23, 14], aiming to reduce the spatial ambiguity. The basic concept was minimization of the inter-element spacing redundancy in order to increase the overall resolution. Although the q-th order statistics based approach promises substantial improvement, both noise sensitivity and impractical computation costs are dominant drawbacks, limiting the usage of such methods in practical applications.

Adaptive processing schemes [10, 18], being a wide and active research area, were also suggested trying to adaptively estimate and suppress the noise component in impinging signals by minimization of the receiver's output energy with some constraints. In [18], two main approaches to adaptive processing are discussed. The block adaptive scheme (which is also called *sample matrix inversion*) and the sample-by-sample method. In both methods, after a certain amount of time, the system refreshes the spatial filter coefficients, trying to better suppress the received noise. As in many adaptive processing applications, the two methods rely on steepest descend optimization, which exposes the adaptive processing approach to errors related to optimization parameters choices such step size etc.

In [36], ULA based beamforming and temporal FIR filtering are shown to be mathematically analogous, where the DOA acts as the spatial version of temporal frequency. Inspired by this analogy, which is thoroughly discussed in Sec. 2.6, we were motivated to find the spatial counterpart of the temporal IIR filter, both from academic curiousness and due to the known advantages of the IIR filter's performance. Therefore we formulated a question, "what are the equivalent spatial domain processing methods which will be analogous to temporal IIR filtering?" which served as a guide throughout our research.

Achieving spatial IIR response has also motivated other works. In [38] two methods were considered. The first one (see Fig. 1.1) was to estimate the time of arrival (TOA) difference between two consecutive sensors and to synthetically generate the recursive part of the IIR filter, entirely in the time-domain. The second approach suggested to consider overlapping subsets of one large ULA as finite approximation to an infinite array (see Fig. 1.2). Obviously, the former approach is very sensitive to the synthetic delay accuracy and involves temporal domain

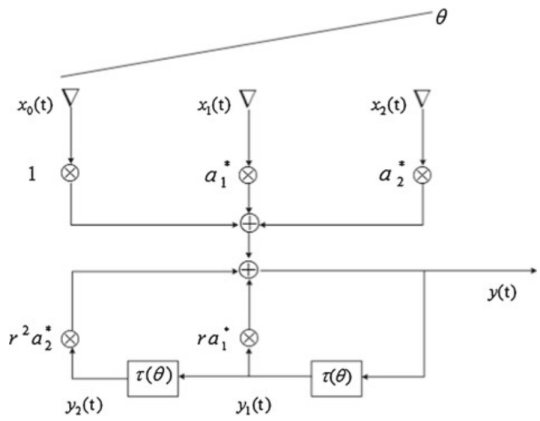

Figure 1.1: Synthetic delay emulated for the recursive part of the spatial IIR filter.

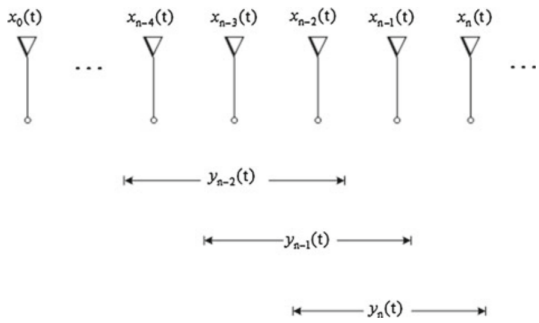

Figure 1.2: In [38] subsections on a single large ULA are used to approximate an IIR response

processing (which we try to avoid in this work in order to achieve purely spatial processing). Also, close inspection of the latter approach reveals that even though the sub-arrays are each weighted separately, each sensor's output is eventually linearly weighted when taking into account all related sub-arrays. Clearly, this is just another possible implementation of basic FIR like ULA spatial processor, so in both cases, there is no true spatial feedback between the array and the source of interest.

Other interesting works [11, 17] in the field of ultra-wideband (UWB) signals treat the spatial and temporal diversity, which reside in multiple consecutive snapshots of the array output, as if the signal is sampled in two independent temporal frequencies. Inspired by [4], the authors show that impinging plane waves are represented as straight lines tilted according to their DOA and suggest methods to design line filters in that spatio-temporal plane. In [11], the authors also address the fact that ideal straight line filter is mathematically unachievable due to spatio-temporal frequencies periodicity. This issue manifests as a "bend" close to the sampling frequencies (see Fig. 1.3).

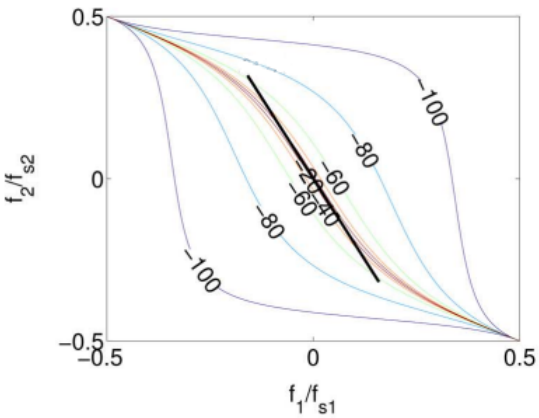

Figure 1.3: 2D spatio-temporal frequency response (dB) of practical UWB filter. The black line is angled according to the desired DOA.

1.2 Overview of the Thesis

In this thesis, we propose a new feedback based beamformer architecture which acts as an actual spatial IIR filter while avoiding any temporal processing to the signal. The reader may observe that the presented research stages lead one to the other as each analysis of the proposed methods uncovered issues that are addressed in the following.

First, as in the early stages of the research, the analogy between a spatial (the ULA) and temporal (the FIR) processors, led us to search for the spatial counterpart of another temporal (the IIR) processor, aiming to transfer its advantages from the temporal domain to the spatial domain. Also, classic spatial analysis tools have been gathered to serve as performance measures to asses to the proposed solutions.

In the second part of the research we present the basic spatial architecture, called FB, introducing the concept of spatial feedback. The array configuration is rigorously justified, e.g. the setting of the coefficients is done with the use of the Fisher Information Matrix (FIM). Analysis of the spatial structure proves that the desired recursive spatial response is achievable and we show that the advantages of the proposed solution may be expressed within the classical analysis framework. As we aim to present a practical architecture, estimation errors were taken into consideration and unveiled some sensitivities that should have been addressed.

After close inspection, we conclude in the third part that the range estimation errors cause this sensitivity and search for ways to mitigate it. To this end, we present a more sophisticated design, based on the basic architecture, achieving a practical low sensitivity spatial processor which successfully extracts spatial information from two independent close frequency FB units. We then simulate the proposed solution and find that in addition to its low sensitivity, it also outperforms the classic beamformers, such as the conventional beamformer (CB) in low SNR.

1.3 Main Contributions

In this contribution, we present a low-complexity sensor array processing approach which achieves the desired spatial domain exclusive IIR-like beampattern, while avoiding any temporal processing of the signal. To this end, we arbitrarily choose to formulate the problem in the context of localization, hence our goal is to estimate the direction and the range of some target of interest.

The novelty, compared to traditional array processing, is by incorporating spatial feedback, which we prove to be the spatial domain equivalent of temporal domain IIR filtering. Assuming the target of interest has a mirror-like behaviour (i.e., reflects its impinging signals), the spatial feedback between the array and the target is created by continuously re-transmitting a synthesized version of the impinging signal (and its reflections) to the target. Note that the initial stimulus can be generated by the target or the array itself. In the text to follow, we assume this is the latter. Furthermore, as opposed to the passive target case (i.e., a target which merely reflects the impinging signal), one may consider a cooperative target, which receives, enhances and re-transmits the signal back to the array.

1.4 Thesis Organization

This thesis is organized as follows. In Chapter 2, we cover basic concepts of array processing, followed by some emphasize in the field of localization and finalize with the basic concepts which drive the motivation for this research.

In Chapter. 3 the basic FB is presented and thoroughly analysed, followed by the presentation of the more robust architecture, which uses the former as a building block. Simulations are also provided, supporting the analytical analysis.

In Chapter. 4 we discuss the results and conclude our findings. We finalize by also proposing some leads to future research.

Chapter 2

Preliminaries

In this chapter, we discuss the theoretical preliminaries for this thesis. First, a short overview of array-processing is presented in Sec. 2.1, accompanied by a complementary wave propagation elementaries in Sec. 2.2. As a preface to spatial filtering, we mention the time-space relation of spatially sampled signals in Sec. 2.3, which is followed by a discussion of classic spatial performance analysis methods in Sec. 2.4 and further elaboration on localization in Sec. 2.5. Finally, Sec. 2.6 reviews the FIR/IIR filters, presents the pros and cons of both architectures and serves as the foundation for this research's motivation.

2.1 Sensor arrays

Sensor arrays are sets of independently positioned sensors, where each sensor is sampling temporal snapshots of impinging signals. The samples from the entire array are then fused together in order to extract the underlying data. The spatial diversity of the sampled data allows the extraction of spatial features. Sensor arrays are used in numerous applications, ranging from source localization, communication, medical applications, astronomy etc.

When designing a sensor array, multiple consideration are to be taken into account, ranging from physical characteristics e.g. area, weight and carrying platform, through performance related considerations such as accuracy, spatial selectivity, SNR and even the financial aspect. The most fundamental array specification is its geometry, for it dictates the spatial relations between simultaneous samples measured by the array's sensors, which also greatly influences the processing methods of the raw-data. A basic example of a sensor array is the ULA (see Fig. 2.1), where its elements are uniformly spaced on a straight line with distance d between each pair of sensors. Considering an array of N elements, the sensors are positioned at

$$p_n = nd, \; n = 0, \ldots, N-1 \tag{2.1}$$

where n is the sensors index; p_n denotes the position of the n'th sensor, $p_0 = 0$ corresponds to the left-hand side of the array as illustrated in Fig. 2.1.

To properly formulate the discussed additional spatial information when using sensor ar-

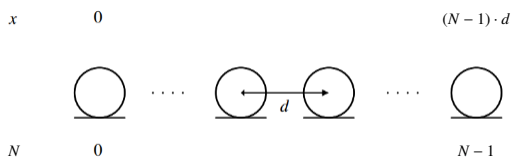

Figure 2.1: A ULA of size N and spacing d.

rays, a quick overview on wave propagation is due and presented in the following section (Sec. 2.2).

2.2 Propagating Wave Fields

An elementary physical phenomenon is the spatial and temporal dynamics of waves, referred to as wave-propagation. The spatial location is noted by the Cartesian coordinates (x, y, z) or the three dimensional spherical coordinates (r, ϕ, θ), where $0 \leq \phi \leq 2\pi$, $0 \leq \theta \leq \pi$ are the azimuth and elevation angles, respectively. The relations between the coordinates are given in Fig. 2.2. Denoting t as the time, the time-space representation of the a signal is $f(t, \boldsymbol{r})$. In a homogeneous, dispersion free and lossless medium the wave equation is:

$$\nabla^2 f(t, x, y, z) = \frac{1}{c^2} \frac{\partial^2 f(t, x, y, z)}{\partial t^2} \tag{2.2}$$

where ∇^2 is the Laplacian operator and c represents the wave's velocity in the medium. A

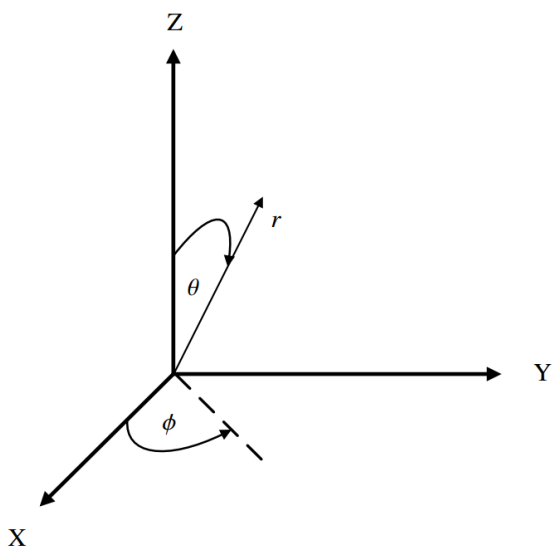

Figure 2.2: A three dimensional coordinate system with Cartesian and spherical coordinates.

possible solution to (2.2), $f_p(t, x, y, z)$, is a complex exponential of the form:

$$f_p(t, x, y, z) = A \exp\left[j\left(\omega t - k_x x - k_y y - k_z z\right)\right] \tag{2.3}$$

Where A is a complex constant, ω denotes temporal radial frequency, $\boldsymbol{k} = \left[k_x, k_y, k_z\right]^T$ denote the *wavelength vector* and k_x, k_y, k_z are real constants. Indeed, plugging (2.3) into (2.2) results in the *monochromatic plane wave* satisfying:

$$k_x^2 + k_y^2 + k_z^2 = \frac{\omega^2}{c^2}. \tag{2.4}$$

Using the plane wave notation

$$f(t, \boldsymbol{x}) = A \exp j\left(\omega t - \boldsymbol{k}^T \boldsymbol{x}\right), \tag{2.5}$$

where $\boldsymbol{x} = [x, y, z]^T$ emphasizes the fact that for a given time, t_0, all points on a plane given by $k_x x + k_y y + k_z z = constant$ are with the same phase value where $\boldsymbol{k}^T \boldsymbol{x} = constant$ are planes of constant phase value. The wave propagation can be described as the traveling of the planes, stating that small steps of both space $\delta\boldsymbol{x}$ and time δt result in the same wave value i.e. $f(t + \delta t, \boldsymbol{x} + \delta\boldsymbol{x}) = f(t, \boldsymbol{x})$, which yields

$$\omega\delta t - \boldsymbol{k}^T \delta\boldsymbol{x} = 0. \tag{2.6}$$

Assuming $\delta\boldsymbol{x}$ and $\boldsymbol{k}$ have the same direction, $\boldsymbol{k}^T \delta\boldsymbol{x} = |\boldsymbol{k}|\,|\delta\boldsymbol{x}|$ and $\frac{|\delta\boldsymbol{x}|}{\delta t} = \frac{\omega}{|\boldsymbol{k}|}$, where $\frac{|\delta\boldsymbol{x}|}{\delta t}$ can designate the propagation speed of the plane wave. Since $\boldsymbol{k}$ and ω are related by $|\boldsymbol{k}|^2 = \frac{\omega^2}{c^2}$, we have

$$\frac{|\delta\boldsymbol{x}|}{\delta t} = c. \tag{2.7}$$

The *wavelength* (λ) denotes the distance the plane wave propagates during a single temporal period of $T = \frac{2\pi}{\omega}$. Its magnitude $|\boldsymbol{k}|$ expresses the number of cycles in radians per meter of length that the plane wave has exhibited in the propagation direction. Using (2.7) with $\delta t = \frac{2\pi}{\omega}$, we obtain:

$$\lambda = |\delta\boldsymbol{x}| = \frac{2\pi}{|\boldsymbol{k}|}. \tag{2.8}$$

Therefore, the wavenumber vector can be considered to represent spatial frequency, similarly to the manner ω represents temporal frequency.

For example, in the context of ULA, assuming a far field scenario, the impinging waves are treated as constant phase planes as in (2.5). The spatial diversity of the ULA elements is expressed as a TOA difference of the impinging signal in each sensor which will be shown to provide clues for the signal's DOA (measured from the array's broadside) as can be seen in Fig. 2.3. When also considering the narrowband scenario, where TOA difference is merely phase shift, it seems obvious that by measuring phases, one should be able to extract the DOA from the spatially sampled data.

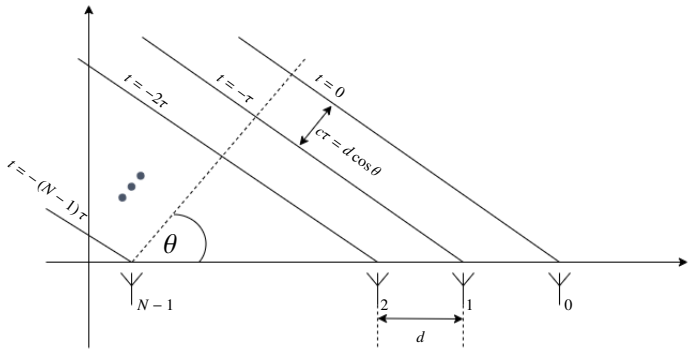

Figure 2.3: An illustration of an N element ULA, impinged with a plane wave arriving from a DOA of θ.

2.3 Spatio-temporal processing

As mentioned before, the measurements of the sensor array's elements are utilized together, where spatial information resides in the relations between samples taken the same time t. A basic application of the sensor array is the beamformer, designed to enhance signals from certain directions while suppressing other signals from unwanted directions, forming a beam directed to the enhanced direction. In complimentary to Fig. 2.3, Fig. 2.4 adds the processor

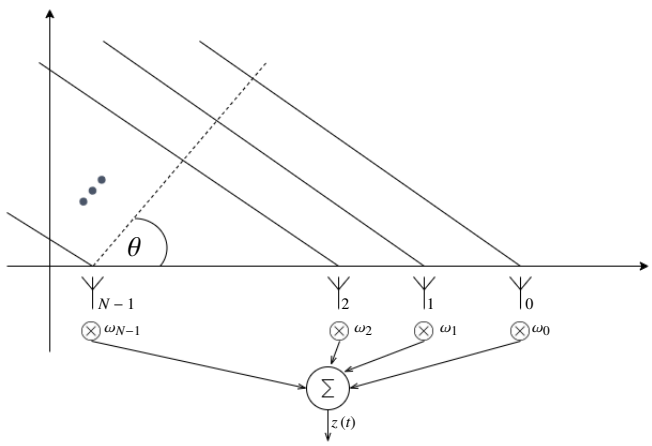

Figure 2.4: ULA based coherent processing of simultaneous spatially sampled signal, measuring a wavefront impinging from DOA θ

layer of the beamformer.

A temporal snapshot measured by the array at time t is

$$\boldsymbol{f}(t, \boldsymbol{p}) = \left[f(t, p_0), \ldots, f(t, p_{N-1})\right]^T . \tag{2.9}$$

Considering the CB [35], the output ($z(t)$) is expressed by:

$$z(t) = \sum_{n=0}^{N-1} f(t, p_n)\, \omega_n^*, \tag{2.10}$$

where ω_n is a complex weight used for the n'th sensor's output, as shown in Fig. 2.4 and * denotes complex conjugation. Consider $s(t) = e^{j\omega t}$ as a plane wave propagating at temporal frequency ω, and $\theta \in \left[-\frac{\pi}{2}, \frac{\pi}{2}\right]$ as the DOA angle measured with respect to the broadside of the linear array, as shown in Fig. 2.4. The wave signal, spatially sampled by the sensor array inputs is

$$\boldsymbol{f}(t, \boldsymbol{p}) = [s(t), s(t-\tau) \ldots, s(t-(N-1)\tau)]^T, \tag{2.11}$$

where $\tau = \frac{d \cdot \cos\theta}{c}$ is the propagation delay between consecutive sensors and c is the wave's velocity in the medium. Considering narrowband signals, the time delay τ translates to a mere phase shift and the *steering vector* takes the form of

$$\boldsymbol{d}(\theta) = \left[1, e^{-j\omega\tau}, \ldots, e^{-j\omega\tau(N-1)}\right]^T. \tag{2.12}$$

It is worth mentioning, that in the general case, the sensor array may be mounted on an arbitrary platform and each sensor may have an arbitrary frequency dependent radiation pattern, such that the steering vector take the form of

$$\boldsymbol{d}(\theta, f) = \left[1, \mu_1(\theta, f)\, e^{\psi_1(\theta,f) - j\omega\tau}, \ldots, \mu_{N-1}(\theta, f)\, e^{\psi_{N-1}(\theta,f) - j\omega\tau(N-1)}\right]^T$$

where $\mu_i(\theta, f)$ and $\psi_i(\theta, f)$ are the frequency and geometrically dependent attenuation and phase of i'th sensor's spatial response. As every impinging signal will cause the excitation of the array elements in the form of a specific steering vector (up to a common additive phase), we define the *array manifold* to be the set of all steering vectors of $\theta \in [0, 2\pi)$, hence it also spans the received signal subspace in the noiseless scenario.

2.4 Array spatial performance

As mentioned in Chapter. 1, array processing serves in many different application, each with its unique requirements, setup and constraints - hence performance criteria are application dependent. In this work, we focus on localization related applications and suggest a new architecture for the beamformer design. Hence, to analyse the presented scheme, we use classic localization-related performance metrics.

To this end, we follow the classic [35] performance analysis, elaborated in the following. Those criteria are then used to quantify the presented architecture's performance in Chapter. 3.

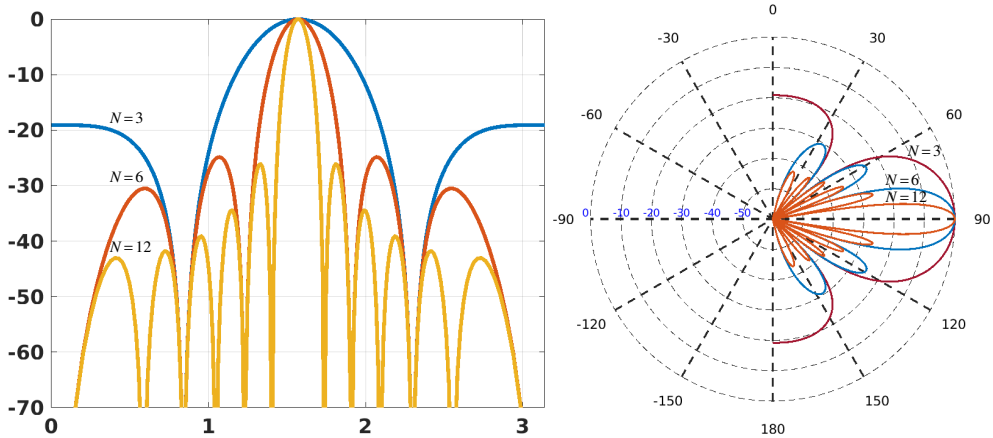

(a) (b)

Figure 2.5: Two common ways of visualizing the array's response in the 2D planar case. In both plots, a comparison between the CB's responses of 3,6 and 12 elements arrays is simulated. In Fig. 2.5a, the response is presented on the $[0, \pi]$ interval with units of dB. In Fig. 2.5b, a polar plot is presented with same units for the response gain but the DOA is in degrees.

2.4.1 Beampattern

Considering DOA estimators, the main tool for assessing an array's localization performance is expressing it's response to impinging signals with various DOA. For sensors in 3D space the DOA depends on two angles (azimuth and elevation). However, for the sake of simplicity, we consider a planar (i.e. azimuth without elevation) DOA such that the beampattern is a function of an angle θ

$$B(\theta) = |Z(\theta)|. \tag{2.13}$$

The beampttern is commonly presented in a graphical manner with log scale as exemplified in Fig. 2.5. It's characteristics, such as main lobe width, position and attenuation of sidelobes are then analysed and compared between different schemes. The analysis can be done theoretically, when the beampattern's mathematical expression is known or it can be conducted numerically. The DOAs of the impinging signal may be presented in various ways where units may be degrees or radians. In this work, we choose to follow [35]'s ψ-space, i.e.

$$\psi(\theta_d) = \frac{2\pi}{\lambda} \cos\theta_d \cdot d, \tag{2.14}$$

where λ is the impinging signal's wavelength.

2.4.2 The normalized beampattern

As the absolute output gain is system dependent, comparing two different beampatterns is not possible where their maximal gain of the mainlobe are different. Therefore, a common practice [35] when analysing the array's spatial performance, is to normalize the beampattern such that the mainlobe's output gain at it's peak is 1 (0dB), thus enabling convenient comparable

measures extraction. This quantity will be referred to as

$$\mathcal{H}(\theta) = H(\theta)/H(\theta_s)$$

where H is the array's response and θ_s is the DOA that the array is steered to.

2.4.3 Half power beamwidth

Considering localization problems, the spatial resolution is obviously linked to the main lobe's width, i.e. higher resolution is achieved for narrower main lobe. The Half Power BeamWidth (HPBW), marked as $\Delta\theta_{HPBW}$, is defined to be the 3-dB beamwidth, i.e. the point where $|B(\theta)|^2 = 0.5$ or $|B(\theta)| = 1/\sqrt{2}$. For standard N-element ULA, assuming large N values, it is known [35] that

$$\Delta\theta_{\mathrm{HPBW}}/2 = 1.4/N. \tag{2.15}$$

Obviously, we aim to show that the presented architecture increases the resolution, compared to other arrays by proving that the beamwidth shrinks below the $1.4/N$ limit.

2.4.4 Sidelobes attenuation

A known [35] parasitic phenomenon of beampatterns is sidelobes, which manifests as energy peaks outside the mainlobe, typically highest near the mainlobe and decreasing towards the edges of the beampattern. In the context of localization, this can cause false detection or reduction in spatial resolution. Related spatial performance metrics are the sidelobes gain and rate of decrease in sidelobe gain.

2.4.5 Directivity

A common measure of performance of an array or aperture is the directivity $\mathcal{D}$. As in [35], in a transmitting array, $\mathcal{D}$ represents the maximum radiation intensity (power per DOA) divided by the average radiation intensity (averaged over all DOAs). Also, in a receiving array, the denominator represents the noise power at the array output due to isotropic noise (noise distributed uniformly over all DOAs). The numerator will represent the power due to a signal arriving from a certain DOA (θ_d) - Thus, $\mathcal{D}$ can be interpreted as the array gain against isotropic noise. We define the power pattern, $P(\theta_d)$, to be the squared magnitude of the beampattern $B(\theta_d)$

$$P(\theta_d) = |B(\theta_d)|^2 \tag{2.16}$$

where the frequency dependence is suppressed. Then the directivity $\mathcal{D}$ is defined as

$$\mathcal{D}(\theta_d) = \frac{P(\theta_d)}{\frac{1}{2\pi}\int_0^{2\pi} P(\theta)\, d\theta}. \tag{2.17}$$

and for uniformly weighted ULAs, it is known [35] that $\mathcal{D} = N$.

2.5 Localization

In the wide and very active research field of parametric estimation, one issue of relevance to this thesis is localization.

In this work, we focus on localization of signal sources in the far-field case, where free space signal propagation is assumed. Following the classical methods overview in [13], localization estimators may be divided to two main groups - *spectral-based* and *parametric*. The spectral based estimators steer the array (mechanically or by beamforming) to a set of DOAs, searching for peaks in the received energy, where each peak is treated as a resolved emitter when greater than a certain threshold. This approach of spatial filtering, is considered to suffer from fundamental limitations, namely "its performance, is directly dependent upon the physical size of the array (the aperture), regardless of the available data collection time and signal-to-noise ratio" [13]. Although trials were made to increase the resolution of an array given a certain aperture, this limitation remained intact. In this contribution we tackle this issue as will be shown in Chapter. 3 by introducing a spatial feedback.

The later approach, of parameter estimation, assumes a physical model of the experimental scenario. Such methods, not only enabled the increase of spatial filtering resolution, but also allowed the implementation of data processing algorithms, which are more sophisticated than a mere search with a steered array. In the following, a basic overview of some classical algorithms is presented.

The earliest localization algorithms, which date back to world war II, are beamforming based, e.g. the conventional Bartlet [35] and Capon's [5] beamformers. Early examples of parametric estimators, are the Maximum-Likelihood [16, 28] and Maximum-Entropy [1] which assume a known PDF to the received signal and estimate the desired parameters according to sampled data and fitting the closest matching PDF. Until the mid- 1970's, direction finding techniques required knowledge of the array directional sensitivity pattern in analytical form, and the task of the antenna designer was to build an array of antennas with a prespecified sensitivity pattern.

Trying to relax the need for such accuracy, also serving as the origin of the subspace based approach, was the Multiple SIgnal Classification (MUSIC) [27] algorithm. MUSIC essentially relieved the designer from designing accurate radiation patterns by introducing the concept of array calibration. Although MUSIC did not mitigate the computational complexity of solution to the DOA estimation problem, it did extend the applicability of high-resolution DOA estimation to arbitrary arrays of sensors. An important breakthrough, was the introduction of the orthogonal array manifold noise spaces, thus allowing the use of orthogonal projection in order to mitigate the noise effects.

Another important parametric approach related algorithm, is the ESPRIT (Estimation of Signal Parameters via Rotational Invariance Techniques) [26], serving as a milestone in the path to state-of-the-art algorithms. In addition to using the rotational invariance of the signal subspace eigenvectors, it also reduced computation and storage costs (especially in the multi-dimensional estimation case) by replacing the covariance matrix calculation and eigen-

decomposition by a relaxed partial singular value decomposition (SVD) which is employed on the data itself without squaring it - thus mitigating numerical problems associated with ill-conditioned matrices.

Following state-of-the-art developments [33], the subspace based algorithms are still modified and adjusted to specific scenarios as in [43] but also new and interesting approaches emerged such as

- High Order Statistics (HOS), which extracts more information from the samples' higher order moments, is a very active field of research due to some fundamental issues which are inherently resolved - i.e. the Gaussian noise vanishes in the 4th order statistics and the ability to resolve more DOAs than array elements [7]. This approach, being costly in computation effort, became popular probably due to the recently available low-cost powerful computation platforms.

- Inspired by the vast research field of sparse representations, some algorithms [20] use L^p norms (where $p < 2$), in order to improve estimation resolution under high reverberation acoustic scenarios.

- A very wide and active research field is the concept of cooperative localization related to mobile networks is growing at a very high rate due to the never-ending need for high-bandwidth and low-power communication of the mobile networks.

- Naturally, also many trials of harnessing the promising concept of neural networks are being done, see for example [29].

In this work, we actually revisit the most basic approach - i.e. beamforming which resides under the spectral based algorithms.

2.6 The analogy between array processing and temporal digital filtering

A basic design entity in every signal processing scheme is the digital filter, which is the modern evolution of analog filters. The design of the digital filters is very well established and thoroughly studied research field. As stated in [21] (and numerous other sources), two key filter types are FIR and IIR filters. This section will briefly overview the design methods and the analogy of ULA based beamforming to the temporal FIR filtering, as implied in Chapter. 1.

- **FIR design**
  The FIR filter is a merely a delay-and-sum mechanism, therefore its memory is finite and equals to the number of taps in the final filter's configuration as in Fig. 2.6.

- **IIR design**
  IIR filters may be viewed as a generalization of the FIR delay-and-sum architecture, where delayed instances of the array's output are fed back to the summation as in Fig. 2.7, generating an infinite loop where each output sample is affected by all past input samples.

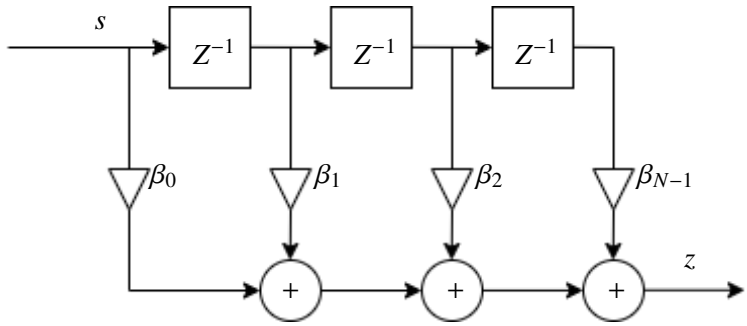

Figure 2.6: An FIR based filtering of signal s with the $\boldsymbol{\beta}$ as the coefficients, generating a filtered signal z.

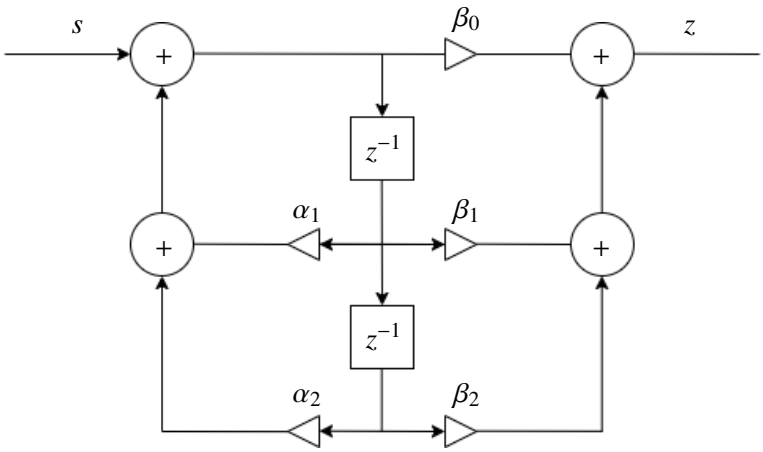

Figure 2.7: Direct form II 2nd order IIR architecture, where the FIR part is the $\boldsymbol{\beta}$ coefficients and the recursive part is implemented via the $\boldsymbol{\alpha}$ set.

In the following, we revisit the basic interpretation of the ULA as the spatial equivalent to the temporal FIR filter [36] where DOA is shown to be the matching spatial entity to the temporal frequency, hence the CB [35] is merely the spatial version of temporal domain FIR filtering.

Let $x_n(t)$ be the measured signal at the n'th sensor

$$x_n(t) = s(t - \tau_n), \tag{2.18}$$

where, $\tau_n = n\tau_{\theta_d} = nd\cos(\theta_\mathrm{d})/c$ represents the time difference of arrival between the n'th sensor and the reference sensor. Defining $\boldsymbol{x}(t) \triangleq [x_0(t) \ldots x_{N-1}(t)]^T$ and its Fourier transform, $\mathrm{X}(\omega) \triangleq [X_0(\omega), \ldots, X_{N-1}(\omega)]^T$, one may write

$$\mathrm{X}(\omega, \theta_d) = \boldsymbol{d}(\omega, \theta_d)\,\mathrm{S}(\omega)$$

where $S(\omega)$ is the Fourier transform of $s(t)$ and $\boldsymbol{d}(\omega, \theta_d)$ denotes the steering vector whose n'th element is

$$d_n(\omega, \theta_d) = \exp(-j\omega\tau_n(\theta_d)). \tag{2.19}$$

Denoting the beamformer's weights as $\boldsymbol{\beta}(\omega)$ and the beamformer's output as z, we express the latter in the frequency domain

$$Z(\omega, \theta_d) = \boldsymbol{\beta}^T(\omega)\, \boldsymbol{d}_{\theta_d}(\omega)\, \mathrm{S}(\omega). \tag{2.20}$$

Defining the electric phase to be

$$\theta = \omega \tau_{\theta_d}, \tag{2.21}$$

we rewrite (2.20) as

$$Z(\omega, \theta) = \mathrm{S}(\omega) \sum_{n=0}^{N-1} \beta_n(\omega) \exp(-jn\theta(\omega)),$$

hence in the ULA case, aiming for a desired spatial response, the weights vector $\boldsymbol{\beta}(\omega)$ configuration is mathematically equivalent to an FIR filter design [36, 3] as illustrated in Fig. 2.8. Assuming narrowband stimuli signals, we suppress ω dependency in the notation throughout

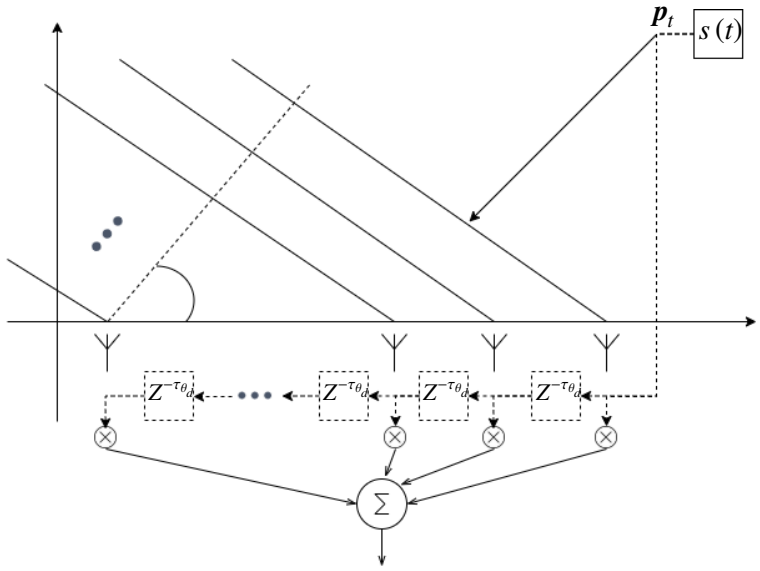

Figure 2.8: An illustration of the analogy between ULA based spatial processing and an FIR temporal filter. The propagation of a plane wave from one sensor to its neighbour (solid tilted lines) is equivalent to the temporal time shift in temporal digital processors (dashed lines and rectangular taps).

the rest of this thesis, where possible.

It is well known [25] that IIR filters have several appealing advantages over their matching FIR counterparts. The main advantage of IIR filters over their FIR counterparts, is their efficiency in terms of the required sensors quantity, which even reaches few orders of magnitude [25] in some cases. In the spatial processing context, this implies improved spatial performance, using the same or smaller number of sensors. However, a well known [21] fact in digital signal processing is that the filter latency may be frequency dependant. When the dependence is linear, it implies that the phase response derivative (i.e. signal latency) is constant such that there is no dispersion. Due to this important property, applications which are sensitive

to signal distortions, especially communication based systems, are based on FIR architecture, for it is possible to design it as linear phase filter. Also notable is the inherent stability of the FIR filter. Nevertheless, motivated by the IIR efficiency, we wish to find the spatial structure that will be analogous to the IIR filter design. To this end, we aim to incorporate a spatial feedback which will serve as the temporal feedback in the IIR architecture (α_1, α_2 in Fig. 2.7) as illustrated in Fig. 2.9.

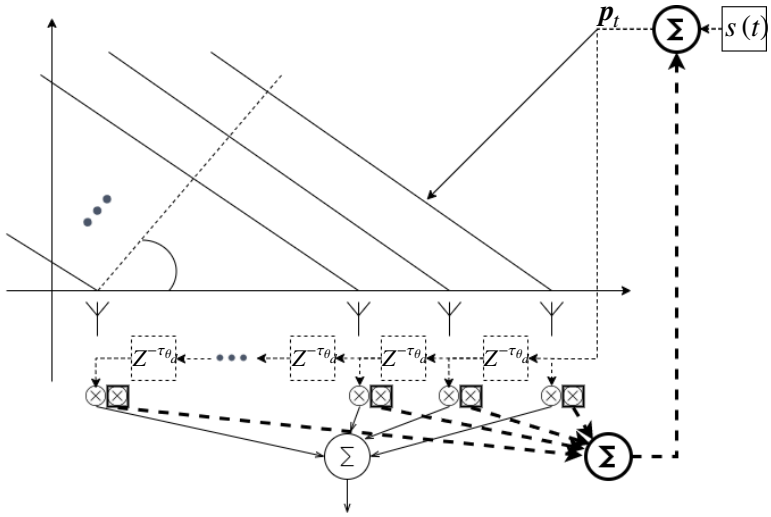

Figure 2.9: An illustration of the spatial feedback concept. On top of the FIR equivalence (non-bold dashed lines), the incorporation of the feedback is presented with the bold dashed lines, generating the "IIR" part of the spatial processor. The multipliers with the bold rectangle wrappers act as the feedback coefficients ($\boldsymbol{\alpha}$) of Fig. 2.7.

In standard radar signal processing schemes, a waveform is transmitted to and reflected from the target of interest. Then, the reflected signal is processed by the radar reception array in order to estimate the target's dynamics (e.g., DOA, range, velocity etc.). As opposed to the standard scheme (as implied from Fig. 2.9) we suggest a continuous re-transmission of the signal and its echoes back to the platform, generating a spatial feedback loop between the array and the target.

Chapter 3

Source Localization with Feedback Beamforming

In this chapter, we revisit the most basic DOA estimation approach, i.e. beamforming, and present our novel feedback based architecture. The feedback based beamforming concept is elaborated in Sec. 3.1. Then, we apply information theory related reasoning for the array setting in Sec. 3.2, namely we use the FIM to design the coefficients of the suggested beamformer. The resultant beamformer's temporal response and spatial performance are analysed in Sec. 3.3 and Sec. 3.4 respectively, assuming ideal noiseless scenario. Considering noisy setups, the beamformer's noise sensitivity is exemplified in Sec. 3.5, followed by a practical and robust dual-frequency beamformer design which is presented in Sec. 3.6.

3.1 Notations and problem setup

In this section, a feedback-based architecture is proposed for spatial signal processing. Inspired by time domain "Direct form II" IIR filter design (see Fig. 2.7), we propose to use the same concept in the spatial domain. The suggested FB architecture, where the output signal (z) is synthesized using weights $\boldsymbol{\beta}$ and the weights $\boldsymbol{\alpha}$ synthesize the feedback transmission ($\mathrm{T_x}$), is presented in Fig. 3.1. The beamformer's output and the feedback signal are synthesized using two independently configured beamformers, s is the system's stimulus and an additive noise (n) is assumed at the array's output. Also, the FB block is marked (dashed line) for later use. Note that setting $\boldsymbol{\alpha} = \mathbf{0}$ (i.e., cancelling the feedback) degenerates the system to the conventional beamformer (CB).

3.1.1 Obtained spatial response

As in Sec. 2.6, an N-element array is considered and some notations are revisited for an easier reading of this chapter. The array's n'th sensor is positioned at $\boldsymbol{p}_n$, for $n = 0, \ldots, N-1$ and we set $\boldsymbol{p}_0$ as the axis reference point while the target of interest is positioned at $\boldsymbol{p}_\mathrm{t}$ and define its distance from the array as $R = \left\|\boldsymbol{p}_\mathrm{t} - \boldsymbol{p}_0\right\|$. The gain of the reimpinging signal is denoted as

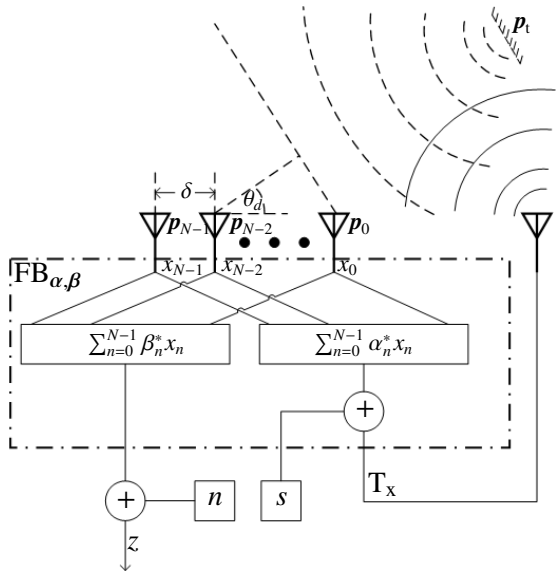

Figure 3.1: The proposed FB. The spatial feedback is obtained by continuous re-transmission of T_x to the target at $\boldsymbol{p}_t$. We designate the FB block (dashed line) for later use.

g which encapsulates both propagation related attenuation and the target's radar cross section (RCS). We also place a transmitter at $\boldsymbol{p}_0$. The transmitted signal s, is reflected back from the target and re-impinges the array with a total delay of $\tau_{\text{pd}} = 2R/c$ seconds, denoting c as the propagation velocity of the signal in the medium. Time domain analysis of the proposed feedback based architecture, considering both propagation delay and attenuation, gives rise to

$$x_n(t) = g\left[s\left(t - \tau_{pd} - \tau_n\right) + \sum_{m=0}^{N-1} \alpha_m^* x_m\left(t - \tau_{pd} - \tau_n\right)\right], \tag{3.1}$$

where the first term on the right-hand-side (RHS) represents the contribution of the transmitted waveform $s(t)$ to the n'th array element and the second term represents the feedback contribution of the re-transmitted array signal to this same element. The reader should bare in mind that in the general case, g is complex and may have an arbitrary frequency and spatially dependencies. Also, the target may reflect multiple instances of the impinging signal as its shape may not be flat. Expressing the Fourier transform of (3.1),

$$X_n = g\left\{\mathrm{S}\exp\left[-j\omega\left(\tau_{pd} + \tau_n\right)\right] + \sum_{m=0}^{N-1} \alpha_m^* \mathrm{X}_m \exp\left[-j\omega\left(\tau_{pd} + \tau_n\right)\right]\right\}, \tag{3.2}$$

and its vector from,

$$\boldsymbol{X} = g\left(\mathrm{S} + \boldsymbol{\alpha}^H \boldsymbol{X}\right)\boldsymbol{d}\exp\left(-j\omega\tau_{pd}\right),$$

we find that it can be simplified to

$$\boldsymbol{X} = g\left(I - g\boldsymbol{d}\boldsymbol{\alpha}^H e^{-j\omega\tau_{pd}}\right)^{-1}\boldsymbol{d}\mathrm{S}\exp\left(-j\omega\tau_{pd}\right).$$

We also denote

$$\phi \triangleq \omega\tau_{pd}$$

as the round-trip signal propagation related electrical phase. We use the Sherman-Morrison formula [30], considered to be a result of the Woodbury matrix identity [41], stating that

$$\left(I + \boldsymbol{u}\boldsymbol{v}^T\right)^{-1} = I - \frac{\boldsymbol{u}\boldsymbol{v}^T}{1 + \boldsymbol{v}^T\boldsymbol{u}},$$

where $\boldsymbol{u}, \boldsymbol{v}$ are two $N \times 1$ vectors and I is the identity matrix. Setting $\boldsymbol{u} = -g\boldsymbol{d}\exp(-j\omega\tau)$ and $\boldsymbol{v} = \boldsymbol{\alpha}^*$ gives rise to

$$\begin{aligned}
\left(I - g\boldsymbol{d}\boldsymbol{\alpha}^H \exp(-j\omega\tau)\right)^{-1} &= I + \frac{g\boldsymbol{d}\boldsymbol{\alpha}^H \exp(-j\omega\tau)}{1 - g\boldsymbol{\alpha}^H\boldsymbol{d}\exp(-j\omega\tau)} \\
&= \frac{\left(I - g\boldsymbol{\alpha}^H\boldsymbol{d}\exp[-j\omega\tau] + g\boldsymbol{d}\boldsymbol{\alpha}^H\exp[-j\omega\tau]\right)\boldsymbol{d}}{1 - g\boldsymbol{\alpha}^H\boldsymbol{d}\exp(-j\omega\tau)} \\
&= \frac{\left[I + \left(\boldsymbol{d}\boldsymbol{\alpha}^H - \boldsymbol{\alpha}^H\boldsymbol{d}\right)g\exp(-j\omega\tau)\right]\boldsymbol{d}}{1 - g\boldsymbol{\alpha}^H\boldsymbol{d}\exp(-j\omega\tau)} \\
&= \frac{\boldsymbol{d} + \left(\boldsymbol{d}\boldsymbol{\alpha}^H\boldsymbol{d} - \boldsymbol{\alpha}^H\boldsymbol{d}\boldsymbol{d}\right)g\exp(-j\omega\tau)}{1 - g\boldsymbol{\alpha}^H\boldsymbol{d}\exp(-j\omega\tau)} \\
&= \frac{\boldsymbol{d} + \boldsymbol{\alpha}^H\boldsymbol{d}(\boldsymbol{d} - \boldsymbol{d})g\exp(-j\omega\tau)}{1 - g\boldsymbol{\alpha}^H\boldsymbol{d}\exp(-j\omega\tau)} \\
&= \frac{\boldsymbol{d}}{1 - g\boldsymbol{\alpha}^H\boldsymbol{d}\exp(-j\omega\tau)}
\end{aligned}$$

leading to

$$\boldsymbol{X} = \frac{g\boldsymbol{d}\exp(-j\phi)}{1 - g\boldsymbol{\alpha}^H\boldsymbol{d}\exp(-j\phi)}\mathrm{S}.$$

Let $z = \boldsymbol{\beta}^H\boldsymbol{x} + \mathrm{n}$ be the beamformer's output (see Fig. 3.1), with Fourier transform Z. Considering the noiseless case (i.e., $\mathrm{n} = 0$), the frequency response of the FB is

$$H_{\beta,\alpha} \triangleq \frac{\mathrm{Z}}{\mathrm{S}} = \frac{g\boldsymbol{\beta}^H\boldsymbol{d}\exp(-j\phi)}{1 - g\boldsymbol{\alpha}^H\boldsymbol{d}\exp(-j\phi)}. \tag{3.3}$$

Note that this architecture achieves a controllable (via setting of $\boldsymbol{\beta}$ and $\boldsymbol{\alpha}$) and recursive (non-trivial denominator) spatial response. As will be shown, high directivity and narrow beamwidth are obtainable by a proper selection of the weights. Compared to traditional beamformers (i.e., without feedback), the performance improvement will be expressed in terms of increased aperture, narrower beamwidth and improved sidelobe attenuation. One may observe that opposed to traditional beamformers, the array response, $H_{\beta,\alpha}$, is not only influenced by the impinging signal DOA, since it is also range selective due to its ϕ dependency. As demonstrated in Fig. 3.2, the combination of both angular and range selectivity enables the designer to enhance signals arriving from specific locations (grey area) rather than only specific directions.

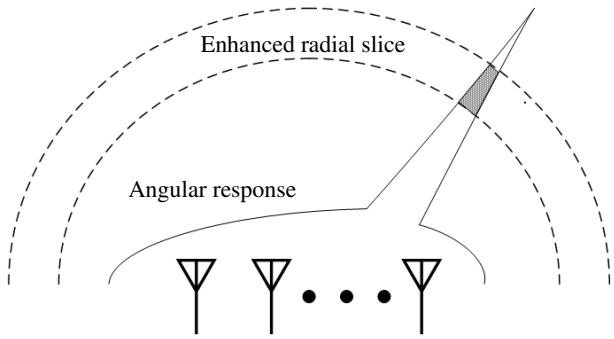

Figure 3.2: Combining both radial selectivity and DOA-based selectivity allows to localize the target.

3.2 Fisher Information Matrix

A possible evaluation for the contribution of the presented feedback mechanism is to measure the additional information in the system. To this end, the FIM (see App. A), denoted by $\boldsymbol{J}$, will now be calculated with respect to the DOA (θ_{d}) and range (ϕ) parameters. As the feedback-based transfer function (3.3) is expressed in the frequency domain, we rely on [42] to express the frequency domain FIM as well.

The $[k, l]$'th FIM element, may be expressed as

$$\begin{aligned} J_{k,l}(\boldsymbol{\eta}) =& \Re\left\{\frac{1}{2\pi}\int_{-\omega_s/2}^{\omega_s/2}\frac{1}{\Phi(\omega)}\mathfrak{F}^*\left\{\frac{\partial z(t)}{\partial \eta_k}\right\}\mathfrak{F}\left\{\frac{\partial z(t)}{\partial \eta_l}\right\}d\omega\right\} \\ &+\frac{T}{4\pi}\int_{-\omega_s/2}^{\omega_s/2}\frac{1}{\Phi^2(\omega)}\left(\frac{\partial \Phi(\omega)}{\partial \eta_k}\right)^*\frac{\partial \Phi(\omega)}{\partial \eta_l}d\omega \end{aligned} \tag{3.4}$$

where $\boldsymbol{\eta} = [\theta_{\mathrm{d}}, \phi]^T$ is the parameters vector, $\Re$ stands for the real-part extraction operator, $k, l \in \{1, 2\}$, $\Phi(\omega)$ is the noise spectrum, $\mathfrak{F}$ is the Fourier transform operator, T is the measurement observation interval and ω_s is the signal bandwidth. For simplicity, $\mathrm{n}(t)$ is assumed to be white Gaussian with some constant power spectral density $\Phi(\omega) = \sigma^2$ and independent of the estimated parameters $\boldsymbol{\eta}$. Hence, the second term in the RHS of (3.4) vanishes. Assuming continuously differentiable functions, where order alteration of the Fourier transform and the differentiation operations is allowed, (3.4) simplifies to

$$J_{kl}(\boldsymbol{\eta}) = \Re\left\{\frac{1}{2\pi\sigma^2}\int_{-\omega_s/2}^{\omega_s/2}\left(\frac{\partial \mathrm{Z}(\omega)}{\partial \eta_k}\right)^*\frac{\partial \mathrm{Z}(\omega)}{\partial \eta_l}d\omega\right\}. \tag{3.5}$$

Expressing the steering vector derivative with respect to θ_{d}, results in

$$\frac{\partial \boldsymbol{d}}{\partial \theta_{\mathrm{d}}} = \boldsymbol{A}\boldsymbol{d} \tag{3.6}$$

where $\boldsymbol{A}$ is an $N \times N$ diagonal matrix with

$$A_{ii} = -j\omega \frac{\partial \tau_i}{\partial \theta_{\mathrm{d}}} \quad \forall i \in \{0 \ldots N-1\}.$$

It is worth mentioning that (3.6) is relevant even for arbitrary arrays (not necessarily ULA) when smooth and slowly changing radiation patterns are assumed. In App. B we compute the FIM terms, concluding that

$$\begin{aligned} J_{11} &= J_{\theta_{\mathrm{d}}\theta_{\mathrm{d}}} = \frac{1}{2\pi\sigma^2} \int_{-\omega_s/2}^{\omega_s/2} \frac{\left|g\boldsymbol{\beta}^H \boldsymbol{A}\boldsymbol{d} - g^2 \boldsymbol{\beta}^H B \boldsymbol{\alpha}^* \exp(-j\phi)\right|^2}{\left|1 - g\boldsymbol{\alpha}^H \boldsymbol{d} \exp(-j\phi)\right|^4} \left|\mathrm{S}(\omega)\right|^2 d\omega \\ J_{22} &= J_{\phi\phi} = \frac{1}{2\pi\sigma^2} \int_{-\omega_s/2}^{\omega_s/2} \frac{\left|g\boldsymbol{\beta}^H \boldsymbol{d}\right|^2}{\left|1 - g\boldsymbol{\alpha}^H \boldsymbol{d} \exp(-j\phi)\right|^4} \left|\mathrm{S}(\omega)\right|^2 d\omega. \end{aligned} \tag{3.7}$$

where $\boldsymbol{B} \triangleq \boldsymbol{d}\boldsymbol{d}^T \boldsymbol{A} - \boldsymbol{A}\boldsymbol{d}\boldsymbol{d}^T$. Aiming to maximize the FIM diagonal elements via denominator (i.e., $\left|1 - g\boldsymbol{\alpha}^H \boldsymbol{d} \exp(-j\phi)\right|$) minimization, the optimal feedback weights are

$$\boldsymbol{\alpha}^*_{\mathrm{CB,opt}} = \frac{\boldsymbol{d}^* \exp(j\phi)}{\hat{g}\, \|\boldsymbol{d}\|^2}, \tag{3.8}$$

where $\hat{g}$ is the channel gain estimate. Considering narrowband signals, this choice of weights may be interpreted as a generalized version of the CB [35] which is a mere coherent summation of the feedback signal. Furthermore, setting $\boldsymbol{\beta} = \boldsymbol{\beta}_{\mathrm{CB,opt}} = \boldsymbol{\alpha}_{\mathrm{CB,opt}}$, is shown (see App. B) to nullify the FIM cross terms, such that $J_{12} = J_{\theta_{\mathrm{d}},\phi} = J_{21} = J_{\phi\theta_{\mathrm{d}}} = 0$.

Note that setting the feedback weights as in (3.8) requires perfect knowledge of the target's range, since ϕ is range dependant. Also, the reader may notice that assuming $\hat{g} = g$, this choice of optimal weights nullifies the denominator of (3.3). Thus, theoretically, the FIM becomes infinite when the transfer function (3.3) is unstable due to positive and coherent feedback between the beamformer and the target. In practice, though, there will be unavoidable errors, and perfect knowledge of target's location and the channel gain is usually unknown. In Sec. 3.4, we quantify the effect of such errors and discuss its influence on the array performance.

3.3 Temporal Stability

As a preliminary, we start with simple temporal simulations of the feedback beamformer. We first address the temporal stability of the system and discuss its correspondence with the system's response which was found in (3.3).

3.3.1 Gain mismatch

The analogy of the FB to the temporal IIR architecture raises some fundamental issues that should be addressed. In the following, supported by simulations, we answer those questions.

The first question, related to the FB's analogy to the temporal IIR architecture, is stability

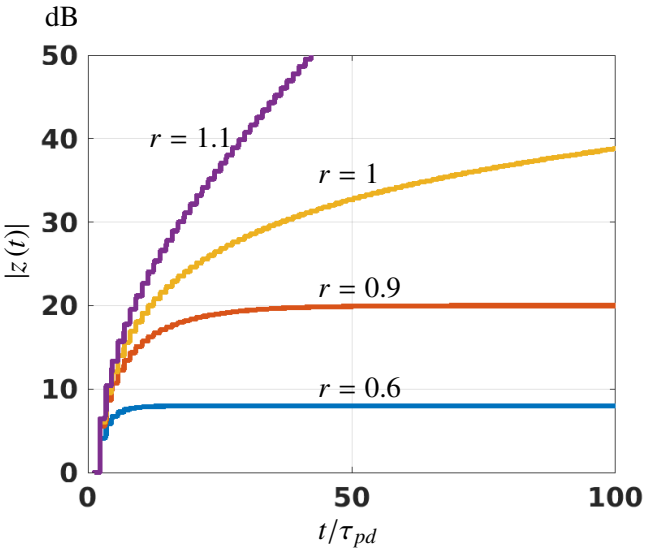

Figure 3.3: Simulating a 3 element ULA based FB, steered to a target which resides in the direction $\theta_s = \pi/2$ and plotting temporal response (dB) for multiple r values. The horizontal axis (t/τ_{pd}) is the time, normalized to the signal's round-trip duration to the target and back.

related. To begin with, we should first ask what does "stability" means. In the absence of any previous related work on spatial feedback, we find that the commonly used Bounded-Input-Bounded-Output (BIBO) stability is appropriate. To this end, the gain mismatch is

$$r = g/\hat{g}. \tag{3.9}$$

And plugging (3.8) into (3.3), gives rise to

$$\begin{aligned} H_{\boldsymbol{\beta}_{\mathrm{CB,opt}},\boldsymbol{\alpha}_{\mathrm{CB,opt}}} &= \frac{g\boldsymbol{\beta}_{\mathrm{CB,opt}}^H \boldsymbol{d} \exp(-j\phi)}{1 - g\boldsymbol{\alpha}_{\mathrm{CB,opt}}^H \boldsymbol{d} \exp(-j\phi)} \\ &= \frac{r}{1-r} \triangleq H_0. \end{aligned} \tag{3.10}$$

As anticipated from (3.10) and confirmed with the simulations presented in Fig. 3.3, for $r \geq 1$ the system is not stable, for the received amplitude may increase (in absolute value) to infinity. In Fig. 3.5, we plot the final amplitude value after 100 iterations of the signal being retransmitted between the array and the target of interest and find that the final values substantially increase as $r \to 1$. This issue will have to be taken into consideration when one designs such an array for practical applications but currently this is outside the scope of this work. As a final observation, we address the "discrete" behaviour of z, i.e. the value (most noticeable in the $r = 1.1$ plot in Fig. 3.3) seems to be piecewise constant. This phenomenon corresponds with the propagation latency of the signal's round trip to the target and back. In each iteration the mainlobe sharpens, as can be seen in Fig. 3.4. The reader may notice in Fig. 3.4 that the $t = 1 \cdot \tau_{pd}$ plot is actually the conventional beampattern, for the feedback signal has not yet re-impinged the array.

The second question to be asked regards the settling time of the system. For example, in Fig. 3.3 we easily observe that the settling time for $r = 0.6$ ($\sim$ 10 signal round trips) is

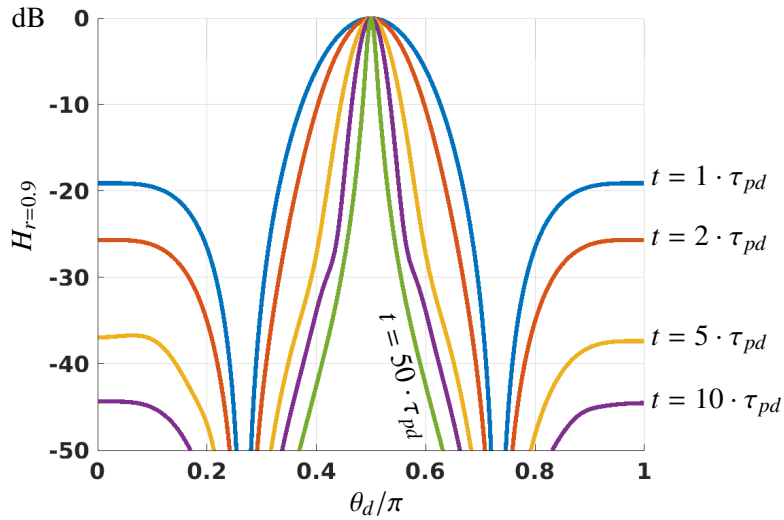

Figure 3.4: Simulation of the same setup as in Fig. 3.3 with $r = 0.9$. Several simulations are conducted, where each is simulated with different duration. It actually illustrates the forming of the final beampattern in time as our analysis assumes infinite duration. This convergence is analogous to the settling time of the IIR filters' temporal response, where at early stages, the response is not yet in its steady-state.

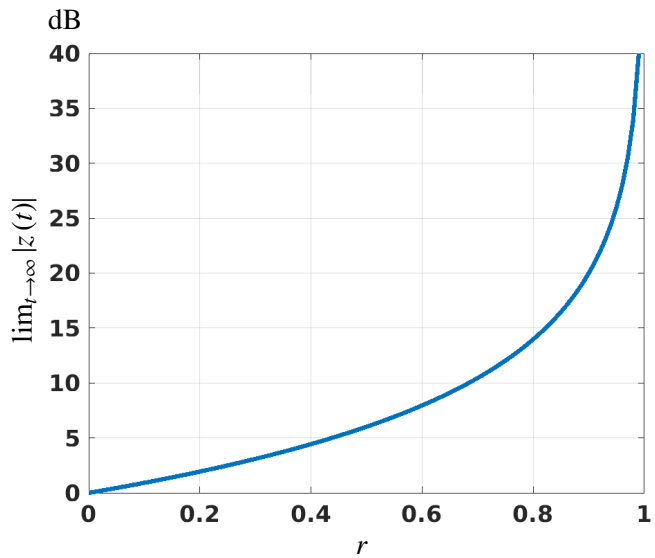

Figure 3.5: After simulating the same setup as in Fig. 3.3, we plot the final received amplitude in dB with different choices of r.

substantially shorter than its matching value (~ 50) when $r = 0.9$. To better understand the phenomenon, we plot for each r value, its corresponding settling time in Fig. 3.6. Although outside of this work's scope, this issue will obviously be of great importance when considering dynamic targets, as will be discussed in the "future research" part of the concluding Chapter. 4.

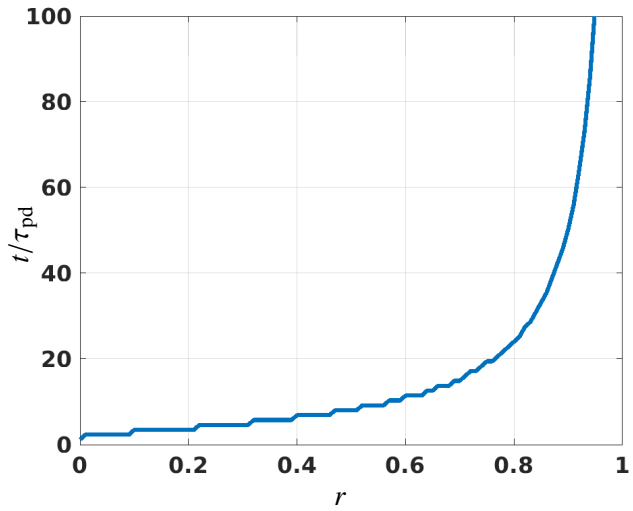

Figure 3.6: Simulation of same setup as in Fig. 3.3. For each r (the horizontal axis), we plot the time (the vertical axis) where the received amplitude entered the 1% sleeve around its final value. The plotted time is also normalized in units of τ_{pd} as in Fig. 3.3.

3.3.2 Phase mismatch

We denote $\hat{\phi}, \hat{\theta}$ to be the range and DOA related phase estimates respectively. As we intend to compare the results to [35], we consider a ULA, introducing its estimated steering vector

$$\hat{\boldsymbol{d}} = \left[1, \exp\left(-\hat{\theta}\right), \ldots, \exp\left(-\left(N-1\right)\hat{\theta}\right)\right]^T . \tag{3.11}$$

Observing that

$$\begin{aligned}
\hat{\boldsymbol{d}}^H \boldsymbol{d} &= \sum_{n=0}^{N-1} \exp\left(jn\Delta\theta\right) \\
&= \frac{\exp\left(jN\Delta\theta\right) - 1}{\exp\left(j\Delta\theta\right) - 1} \\
&= \frac{\exp\left(jN\Delta\theta/2\right)}{\exp\left(j\Delta\theta/2\right)} \cdot \frac{\exp\left(jN\Delta\theta/2\right) - \exp\left(-jN\Delta\theta/2\right)}{\exp\left(j\Delta\theta/2\right) - \exp\left(-j\Delta\theta/2\right)} \\
&= \exp\left(j\left(N-1\right)\Delta\theta/2\right) \cdot \frac{\sin\left(N\Delta\theta/2\right)}{\sin\left(\Delta\theta/2\right)}
\end{aligned}$$

and using the definition of the normalized Dirichlet kernel (illustrated in Fig. 3.7)

$$\mathrm{D}\left(x, N\right) = \frac{1}{N}\frac{\sin\left(Nx\right)}{\sin\left(x\right)},$$

we find that for ULA, (3.3) may be expressed as

$$H_{\beta_{\mathrm{CB}},\alpha_{\mathrm{CB}}} = \frac{r\mathrm{D}\left(\Delta\theta/2, N\right)\exp\left\{-j\left[\Delta\phi + \left(N-1\right)\Delta\theta/2\right]\right\}}{1 - r\mathrm{D}\left(\Delta\theta/2, N\right)\exp\left\{-j\left[\Delta\phi + \left(N-1\right)\Delta\theta/2\right]\right\}}. \tag{3.12}$$

In the following, four fundamental scenarios are considered:

- Perfect alignment $\qquad (\Delta\theta = 0\,, \Delta\phi = 0)\,,$

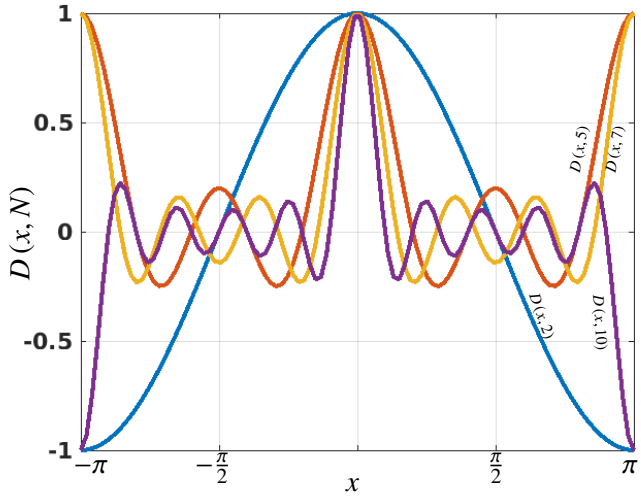

Figure 3.7: Few illustrations of the normalized Dirichlet kernel, for N values of 2,5,7 and 10.

- Steering error $(|\Delta\theta| > 0\,, \Delta\phi = 0)\,,$
- Range error $(\Delta\theta = 0\,, |\Delta\phi| > 0)\,,$
- General $(|\Delta\theta| > 0\,, |\Delta\phi| > 0)\,.$

3.4 Performance Analysis

In this section we analyze the suggested FB (see Fig. 3.1), considering some fundamental properties which are commonly used to asses array performance and were discussed in Sec. 2.4: Beamwidth, peak-to-sidelobe level, and directivity. Each property is then compared to traditional passive ULAs, showing that significantly improved performances are obtainable with spatial feedback integration.

3.4.1 The normalized beampattern

Applying the *normalized beampattern* notation of Sec. 2.4, we set $\boldsymbol{\beta}_{\text{CB}} = \boldsymbol{\alpha}_{\text{CB}}$. Considering the unavoidable errors mentioned in 3.3.2 (i.e. $\Delta\theta, \Delta\phi$ and r), we define $\mathcal{H}_{\Delta\theta,\Delta\phi,r}$ as the general scenario normalized array response. We choose to normalize the spatial response according to H_0 (of (3.10)), giving rise to

$$\begin{aligned}\mathcal{H}_{\Delta\theta,\Delta\phi,r} &\triangleq \frac{H_{\boldsymbol{\beta}_{\text{CB}},\boldsymbol{\alpha}_{\text{CB}}}}{H_0} \\ &= \frac{H_{\boldsymbol{\beta}_{\text{CB}},\boldsymbol{\alpha}_{\text{CB}}}}{r/(1-r)} \\ &= \frac{(1-r)\,\mathrm{D}(\Delta\theta/2, N)}{\exp\{j\,[\Delta\phi + (N-1)\,\Delta\theta/2]\} - r\mathrm{D}(\Delta\theta/2, N)}.\end{aligned} \tag{3.13}$$

Note that the known [35] normalized response of standard ULA is obtained by setting $r = 0$ and $\Delta\phi = 0$

$$\mathcal{H}_{\Delta\theta,\Delta\phi=0,r=0} = \mathrm{D}\left(\Delta\theta/2, N\right) \exp\left(-j\left((N-1)\Delta\theta/2\right)\right).$$

Considering the steering error scenario (i.e., $\Delta\theta \neq 0,\ \Delta\phi = 0$) first, where

$$\mathcal{H}_{\Delta\theta,\Delta\phi=0,r} = \frac{(1-r)\,\mathrm{D}\left(\Delta\theta/2, N\right)}{\exp\left\{j\left[(N-1)\,\Delta\theta/2\right]\right\} - r\mathrm{D}\left(\Delta\theta/2, N\right)}, \tag{3.14}$$

we evaluate the FB's beamwidth, sidelobe level and directivity and compare them to those of the standard ULA.

3.4.2 Half power beamwidth

In App. C we extend the known result of (2.15) for any $r \geq 0$. It turns out that for large N, the HPBW is obtained by solving for x the equality

$$\left(r^2 - 4r + 2\right)\frac{\sin(x)^2}{x^2} + r\frac{\sin(2x)}{x} - 1 = 0 \tag{3.15}$$

where we define $x \triangleq N\Delta\theta_{HPBW}/2$. In Fig. 3.8 we plot the numerical solution of (3.15) for various values of r and N, showing that x reaches its limit around $N = 20$. Also note that for $r = 0$ we obtain the known result of standard ULA with the limiting factor of 1.4. Having the limiting factors for various values of the gain mismatch r, we investigate the feedback related improvement and express the HPBW by

$$\Delta\theta_{\mathrm{HPBW}}/2 \approx \frac{1.4}{f(r)N}.$$

Note that $f(r)$ represents the array aperture improvement factor, compared to the standard ULA. To find a suitable expression for $f(r)$, we computed $\mathcal{H}_{\Delta\theta,\Delta\phi=0,r}$ using $N = 100$ on a fine grid of r values and looked for proper polynomial approximation (using MATLAB®) for the HPBW. It turns out that the 2-nd order polynomial fit satisfies

$$f(r) \approx \frac{1.4}{(1-r)(-0.4r + 1.4)}. \tag{3.16}$$

Note that for an accurate gain match (i.e., $r \to 1$), the RHS of (3.16) tends towards infinity, implying that the equivalent array has an infinite number of elements ($f(r)N$), hence obtaining perfect spatial selectivity (see Fig. 3.9).

3.4.3 Sidelobes attenuation

By taking a derivative of $\mathcal{H}_{\Delta\theta,\Delta\phi=0,r}$ with respect to $\Delta\theta$ it can be easily verified that the beampattern's extrema points are located exactly as in the standard ULA beampattern. Specifically,

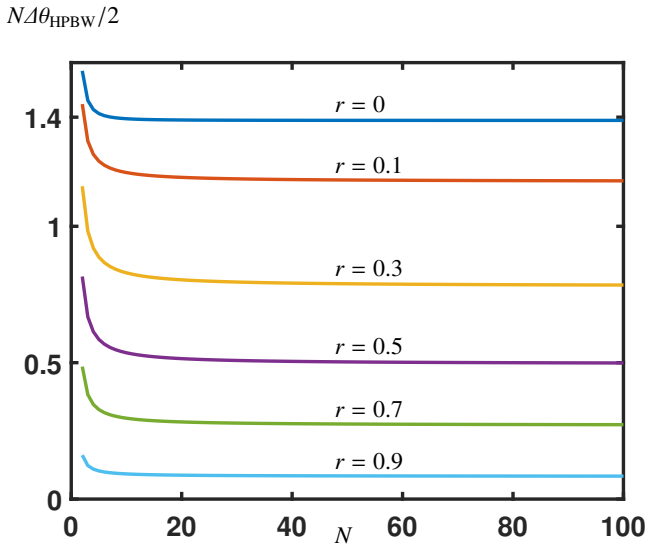

Figure 3.8: Plot of $x = N\Delta\theta_{\mathrm{HPBW}}/2$ vs. N, for various r values, obtained by numerically solving (3.15).

the sidelobes locations are

$$\Delta\theta_{\mathrm{sidelobe}} = \frac{(2m+1)\pi}{N} \ \forall m \in \{\pm 1, \pm 2, \ldots\}. \tag{3.17}$$

Our main interest is with the first sidelobe (i.e. $m = 1$), therefore we evaluate (3.14) at $\Delta\theta = 3\pi/N$, which results in

$$\left|\mathcal{H}_{3\pi/N,0,r}\right|^2 = \frac{2(1-r)^2}{(N^2 - 2Nr)\left(1 - \cos\left(\frac{3\pi}{N}\right)\right) + 2r^2} \tag{3.18}$$

and for large N values

$$\lim_{N\to\infty} \left|\mathcal{H}_{3\pi/N,0,r}\right| = \frac{2(1-r)}{3\pi}.$$

For standard ULA, the gain of the first sidelobe is known to be $2/3\pi$ [35], which implies that the first sidelobe is smaller by a factor of $1 - r$ compared to standard ULA. Specifically, in perfect gain match scenario (i.e., $r \to 1$) , the sidelobes vanish.

3.4.4 Array directivity

In the context of this work, the directivity is expressed as

$$\mathcal{D}(N, r) = \frac{\mathcal{H}_{\Delta\theta=0,\Delta\phi=0,r}}{\frac{1}{2\pi}\int_0^{2\pi} \mathcal{H}_{\Delta\theta,\Delta\phi=0,r}\, d\Delta\theta} = \frac{2\pi}{\int_0^{2\pi} \mathcal{H}_{\Delta\theta,\Delta\phi=0,r}\, d\Delta\theta}, \tag{3.19}$$

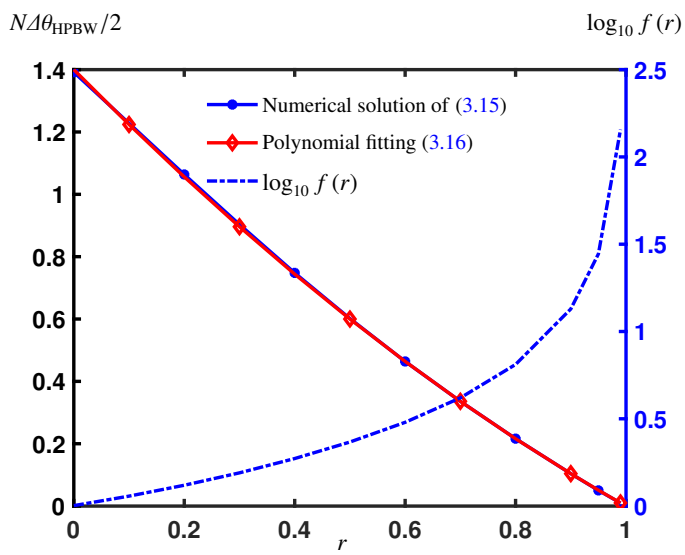

Figure 3.9: Evaluation of $N\Delta\theta_{\text{HPBW}}/2$ for $N = 100$ and its approximation $1.4/f(r)$ (marked by red diamonds). $f(r)$ is also presented, in logarithmic scale (dotted curve).

Plugging (3.14) within (3.19) and by numerical evaluation (see App. D and the complementary Fig. 3.10 and Fig. 3.11) we suggest to approximate the directivity with

$$\mathcal{D}(N, r) \approx \frac{N - r}{1 - r}, \tag{3.20}$$

where the standard ULA's known result is obtained for $r = 0$. Also, for $N \geq 2$, $\lim_{r\to 1} \mathcal{D}(N, r) = \infty$, implying infinite directivity for the perfectly gain-matched FB.

Finally, expressing the improvement in directivity compared to the standard ULA, assuming large N values, gives rise to

$$\lim_{N\to\infty} \frac{\mathcal{D}(N, r)}{\mathcal{D}(N, 0)} = \frac{N/(1 - r)}{N} = \frac{1}{1 - r}. \tag{3.21}$$

3.4.5 Summary

To conclude this section, we summarize the feedback integration related performance improvements in Table. 3.1. Also, in Fig. 3.12 we demonstrate the HPBW and sidelobe attenuation for 3 elements ULA. As the expressions for HPBW and sidelobe-attenuation are relevant for $\sim N > 20$, we also simulate 20 elements ULA in Fig. 3.13. In Table. 3.2 we show the consistency between the results and the performance related expressions of Table. 3.1. As predicted, the results of Fig. 3.13 are consistent with the theoretical expressions.

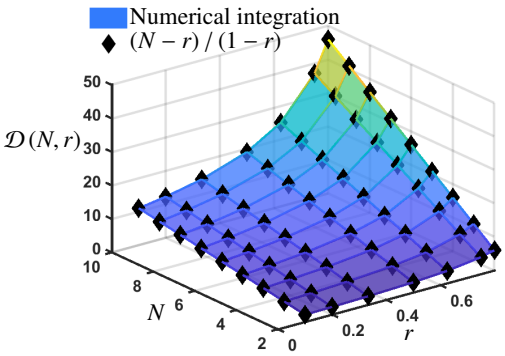

Figure 3.10: Plot of $\mathcal{D}(N,r)$, computed using numerical integration (surface), shown to perfectly match the analytic expression (black diamonds) presented in (3.20).

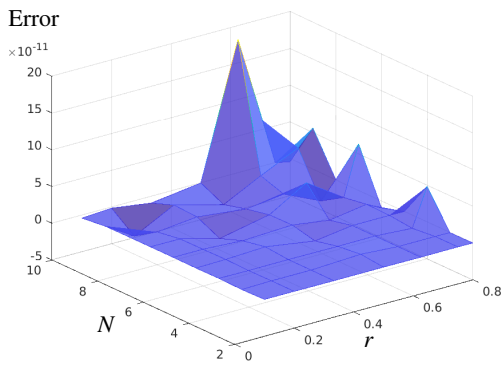

Figure 3.11: The error between numerical calculation and the analytic expression.

Table 3.1: Performances of CB and the Proposed Feedback-Beamforming Architecture, with a Gain Mismatch r.

	CB	FEEDBACK BEAMFORMING	IMPROVEMENT
HPBW	$1.4/N$	$1.4/(f(r)N)$	Narrower by a factor of $f(r)$
FIRST SIDELOBE GAIN	$2/3\pi$	$2(1-r)/3\pi$	smaller by a factor of $1-r$ for $N \gg 1$
DIRECTIVITY	N	$(N-r)/(1-r)$	$1/(1-r)$ times higher for $N \gg 1$

Table 3.2: Performances of CB $r = 0$ and the proposed Feedback-Beamforming Architecture, for several r values. Also comparison to expected theoretical expressions is provided.

	HPBW [RAD]			SIDELOBE GAIN [dB]		
Expected	$\frac{(1-r)(-0.4r+1.4)}{1.4}$			$20\log\left(\left\lvert\frac{2(1-r)}{3\pi}\right\rvert^2\right)$		
	Result	Expected	Error	Result	Expected	Error
$r=0$	0.0605	0.07	0.0095	-26.38	-26.93	0.55
$r=0.3$	0.0454	0.0448	0.006	-32.06	-33.12	1.06
$r=0.6$	0.0259	0.0232	0.0027	-41.21	-42.84	1.63
$r=0.8$	0.0127	0.0108	0.0019	-52.55	-54.88	2.33

3.5 Range Error Sensitivity

In this section, we investigate $\mathcal{H}_{\Delta\theta,\Delta\phi,r}$ for the general case, where the range misalignment phase term $\Delta\phi$ may also be non zero. In Fig. 3.14, we plot $\left|\mathcal{H}_{\Delta\theta,\Delta\phi,r}\right|$ in logarithmic scale, with respect to both steer and range misalignments. Close inspection of the range error related beampattern behaviour sheds light to some important points. First, we notice that although setting $r \to 1$

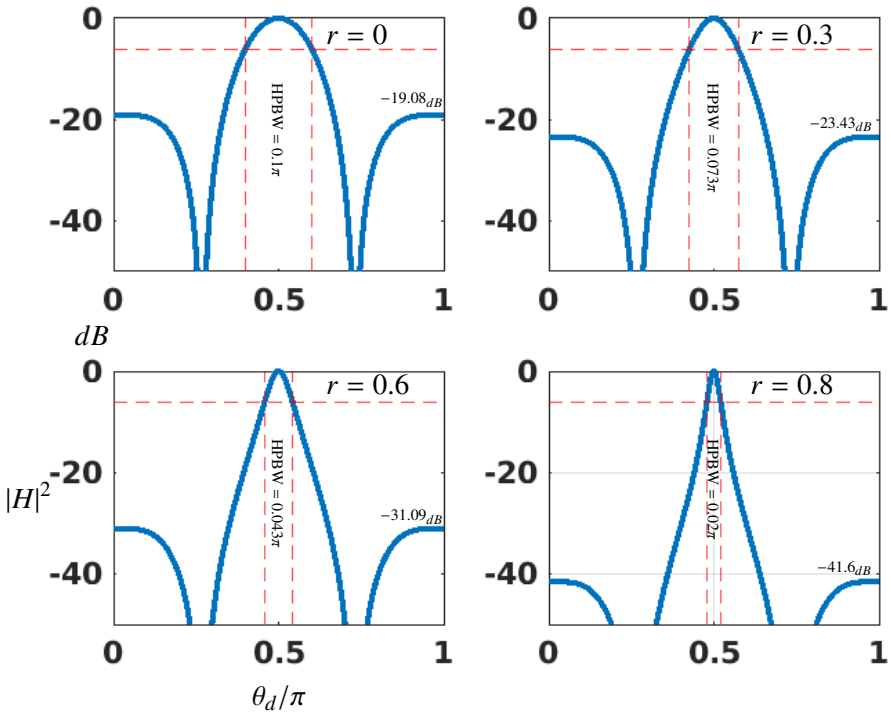

Figure 3.12: Simulating 3 elements ULA based FB for r values of 0, 0.3, 0.6 and 0.8. The HPBW is marked with vertical red dashed line, where an auxiliary horizontal line of $|H|^2 = 1/2$ is also provided. The sidelobe attenuation is cited in each plot in a textual fashion.

(i.e., close to a perfect gain match), sharpens the beampattern's main lobe (i.e., higher spatial selectivity), it also amplifies the range error ($\Delta\phi$) related sensitivity as the main lobe's support over the $\Delta\phi/\pi$ axis shrinks. Next, as evident from (3.13), the range error related sensitivity is 2π-periodic with respect to $\Delta\phi$ (see Fig. 3.15). To establish our final observation, we first recall that

$$\phi \triangleq \omega\tau_{pd} = \frac{2\pi R_{\text{rt}}}{\lambda},$$

where $R_{\text{rt}} = 2R$ is the round-trip distance between the array and the target of interest and λ is the wavelength. Define

$$\Delta R_{\text{rt}} = \frac{\Delta\phi\lambda}{2\pi}$$

to be the range estimation error. Fig. 3.16 shows that even minor range errors of $\Delta R_{\text{rt}} \sim 0.1\lambda$ significantly distort the beampattern.

At first glance, this sensitivity to range errors renders the system being too sensitive for any practical use. This leads us to seek robust implementations, as elaborated in Sec. 3.6.

3.6 Mitigating Range Error Sensitivity

As demonstrated in the previous section, the beampattern (3.13) is sensitive to range errors. We now propose an architecture which obtains the desired beampattern $\mathcal{H}_{\Delta\theta,\Delta\phi\to 0,r}$ even for

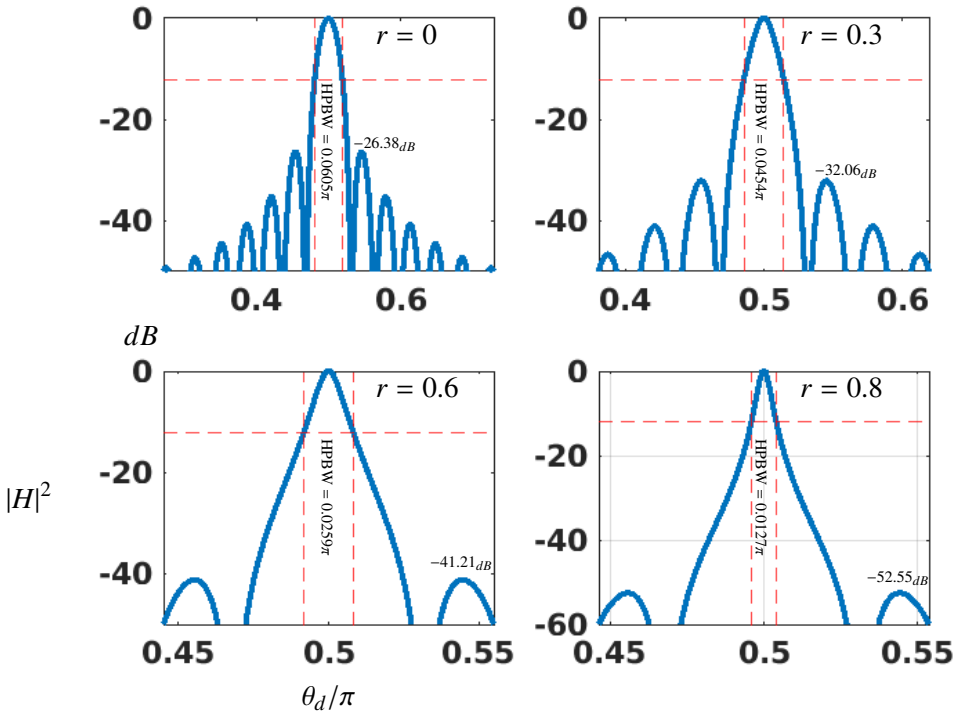

Figure 3.13: Simulating 20 elements ULA for the sake of HPBW analysis. As in Fig. 3.12, r values of 0, 0.3, 0.6 and 0.8 are simulated. The HPBW is marked in the same manner also.

relatively large range errors ΔR_{rt}. Also, we show that the suggested architecture achieves high performance at moderately low signal-to-noise ratio (SNR) scenarios.

3.6.1 Intuition

Bearing in mind that the system's phase alignment sensitivity resides in (3.13) via the term $\exp(j\Delta\phi) = \exp\left(j\omega\Delta\tau_{pd}\right)$ and that the round-trip delay (τ_{pd}) cannot be controlled, one may suggest to use lower frequencies. Unfortunately, aiming for practical range estimation errors, the transmission of such low frequencies is physically unfeasible. Following the thorough spectrum use overview in [2], among the notable considerations for choosing frequency in localization related schemes are

- **Propagation efficiency**
  Due to the chemical structure of the atmosphere, some frequencies are propagated efficiently while other are absorbed [39] by the atmosphere layers, being unsuitable for localization applications such as RADAR.

- **Antenna length**
  As described in [2], although low ($< 30_{\text{KHz}}$) frequencies propagate efficiently in the earth-atmosphere wave guide [39], the wavelength is large ($\sim 10_{\text{Km}}$), hence the needed antenna length is too large for any practical use.

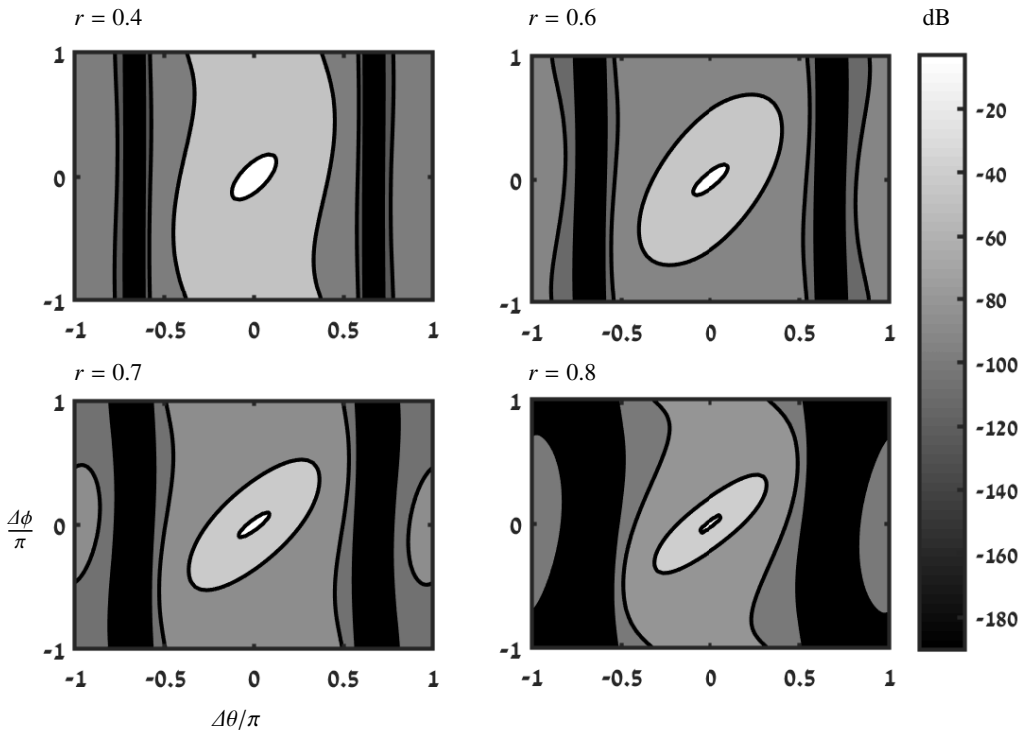

Figure 3.14: Evaluation of $10\log_{10}\left|\mathcal{H}_{\Delta\theta,\Delta\phi,r}\right|^2$, considering both steer ($\Delta\theta$) and range related ($\Delta\phi$) errors. Centered in each plot, is the 3dB main lobe (white color fill), exemplifying that as the gain mismatch r is set closer to one, we observe an increase of the spatial selectivity (regarding both $\Delta\theta$ and $\Delta\phi$).

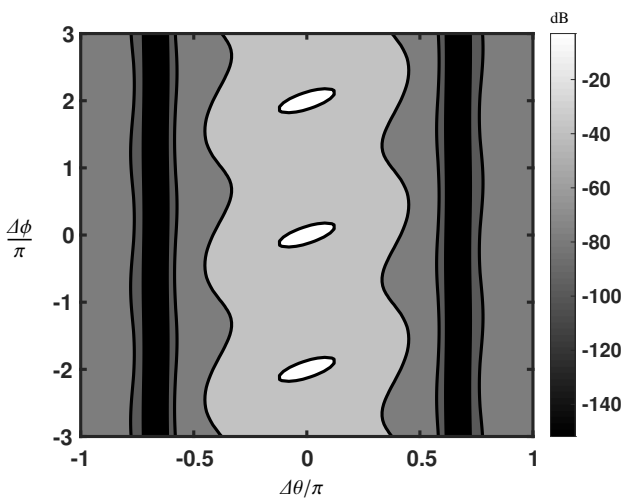

Figure 3.15: Evaluation of $10\log_{10}\left|\mathcal{H}_{\Delta\theta,\Delta\phi,r=0.4}\right|^2$ for $-3\pi \leq \Delta\phi \leq 3\pi$. The response is 2π periodic.

- **Signal bandwidth**

  As the carrier signal's frequency decreases, so does the available bandwidth.

Henceforth, we suggest simultaneous transmission of several frequencies instead of the unfea-

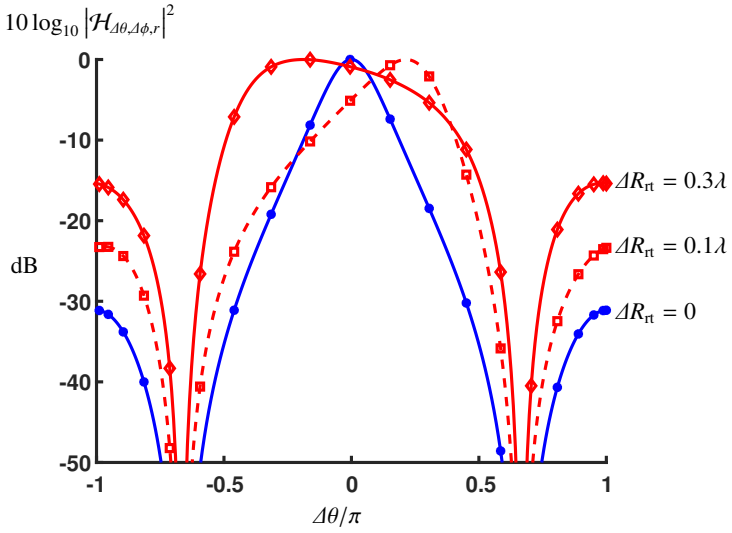

Figure 3.16: Evaluation of the array response (where $r = 0.4$) for several values of range error ΔR_{rt} . Even minor range errors significantly distort the beampattern.

sible option of transmitting low frequencies. In the following we suggest a dual frequency (DF) waveform, utilizing two harmonics, ω_1 and ω_2, and show that range error sensitivity may be resolved as it will depend on the frequency difference $\omega_1 - \omega_2$.

3.6.2 Suggested processing scheme

In Fig. 3.17, we demonstrate the use of two independently configured FB instances (see also Fig. 3.1), where each instance is designed to treat a specific frequency band. A bandpass filter BPF_{ω_i}, $i = 1, 2$ filters a narrowband slice around $\omega_i = 2\pi f_i$. These filters are used to generate both the transmitted feedback signal (Tx_i) and the outputs z_i. The inputs $s_i(t) = \exp(j\omega_i t)$ are the two narrowband stimuli signals and $\mathrm{n}_i(t)$ represents the additive noise.

Note that in the suggested architecture we do not add array elements, but merely double the beamformer processing effort.

For each FB block, its output is given by

$$z_i(t) = H_{\boldsymbol{\beta}_i,\boldsymbol{\alpha}_i}(\omega_i)\exp(j\omega_i t) \quad i \in \{1, 2\},$$

where $\boldsymbol{\beta}_i, \boldsymbol{\alpha}_i$ are the coefficients of the i'th beamformer. Motivated by the desire to mitigate the $\Delta\phi$ dependency of the system, which appears in the denominator of (3.13)'s RHS, we compute the reciprocal of each frequency response, average, and compute the reciprocal again. This leads to the harmonic mean of both beamformers' outputs (see Fig. 3.17), which formally, up to a constant term, takes the form

$$Z_{\mathrm{DF}} = \left|H^{-1}_{\boldsymbol{\beta}_1\boldsymbol{\alpha}_1}(\omega_1) + H^{-1}_{\boldsymbol{\beta}_2,\boldsymbol{\alpha}_2}(\omega_2)\right|^{-1}. \tag{3.22}$$

For convenience, we use subscripts instead of formal ω dependency such that $\phi_i \triangleq \phi(\omega_i)$, $g_i \triangleq g(\omega_i)$, $\boldsymbol{d}_i \triangleq \boldsymbol{d}(\omega_i)$. Also, $r_i \triangleq g_i/\hat{g}_i$ is denoted to be the gain mismatch at ω_i.

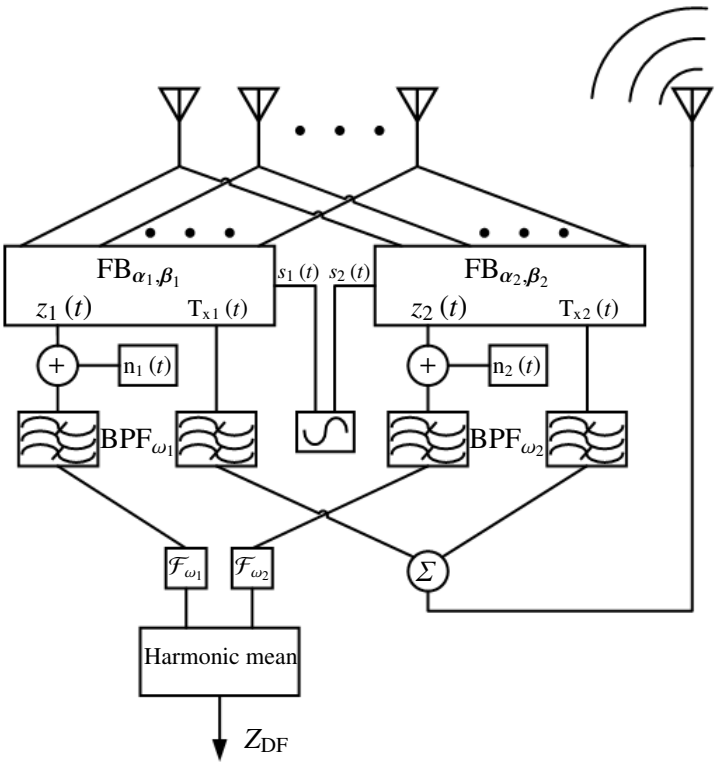

Figure 3.17: DF BF, consisting of two independent FB blocks and narrowband bandpass filters. The blocks marked by $\mathcal{F}_{\omega_i}$ compute the frequency response at ω_i and their outputs feed the harmonic mean calculator, which generates the DF BF's output.

Theorem 3.1. *Consider the architecture suggested in Fig. 3.17, and let $\boldsymbol{\alpha}_i, \boldsymbol{\beta}_i$ be the coefficients of the i'th FB. Then setting*

$$\boldsymbol{\alpha}_1 = \boldsymbol{\beta}_1, \ \boldsymbol{\alpha}_2 = -\boldsymbol{\beta}_2 = [1/\hat{g}_2, 0, \ldots, 0], \tag{3.23}$$

results in

$$Z_{DF} = \left| \frac{g_1 \boldsymbol{\beta}_1^H \boldsymbol{d}_1}{1 - \left(g_1 \boldsymbol{\beta}_1^H \boldsymbol{d}_1 / r_2\right) \exp\left(-j\left(\phi_1 - \phi_2\right)\right)} \right|, \tag{3.24}$$

Proof. See App. E. ■

Assuming close frequencies, Z_{DF} in (3.24) closely resembles the single frequency (SF) beampattern in (3.3), where the range related phase ϕ is now replaced by $\phi_1 - \phi_2 = (\omega_1 - \omega_2)\tau_{pd}$. Hence, one may significantly mitigate the range mismatch distortion of the beampattern by selecting close stimuli frequencies. We also note that throughout the development of (3.24), we did not assume any specific array geometry, hence this result is valid for arbitrary arrays and not just ULA.

3.6.3 Numerical example

Consider a radio frequency carrier of 10 GHz and typical range error of $\Delta R_{\text{rt}} = 10$ m, which is $333\frac{1}{3}\lambda$ (assuming speed of light, $c = 3 \cdot 10^8$ m/s). The single frequency beampattern distortion, being periodic in λ, will closely resemble the 0.3λ error plot presented in Fig. 3.16. Assume that we aim to achieve a maximal phase error of $\Delta\phi = 0.01\pi$. Hence, when using the DF architecture, the dictated frequency separation must satisfy

$$\left|(\omega_1 - \omega_2)\frac{\Delta R_{\text{rt}}}{c}\right| < 0.01\pi. \tag{3.25}$$

or equivalently, for a maximal range error of 10 m, a frequency separation of

$$|f_1 - f_2| < 0.005c/\Delta R_{\text{rt}} = 150\,\text{kHz}$$

is required.

3.6.4 Dual frequency simulation

We now simulate (3.24) for the DF structured FB, generalizing the CB approach and setting

$$\boldsymbol{\beta}_1^* = \frac{\hat{\boldsymbol{d}}_1^* \exp\left(j\left(\hat{\phi}_1 - \hat{\phi}_2\right)\right)}{\hat{g}_1 \left\|\hat{\boldsymbol{d}}_1\right\|^2}.$$

With this choice, denoted as the "DF,CB" beamformer, and similarly to (3.13), (3.24) becomes

$$H_{\text{DF,CB}}(\omega) = \left|\frac{r_1 \mathrm{D}(\Delta\theta/2, N)}{1 - \kappa \mathrm{D}(\Delta\theta/2, N)\exp\left(-j\left(\phi_2 - \phi_1 + (N-1)\Delta\theta/2\right)\right)}\right|, \tag{3.26}$$

where $\kappa \triangleq r_1/r_2$ is the gain mismatch ratio. For close frequencies, one may assume that $r_1 \approx r_2$, hence κ tends towards unity, thus significantly mitigating the gain mismatch effect even when both FBs are mismatched.

Simulating the DF architecture, configured to mitigate range estimation errors as in (3.25) and plotting its normalized (to 0 dB peak gain) beampattern together with the perfectly range aligned scenario, we show in Fig. 3.18 that the DF architecture achieves a near-optimal performance, despite the inherent range error of $\Delta R_{\text{rt}} = 10$ m. In Fig. 3.19, we repeat the simulation while adding white Gaussian noise to the output of each FB. Evidently, even in the noisy case, the DF BF achieves a close-to-ideal beampattern, while the SF BF suffers from severe distortions.

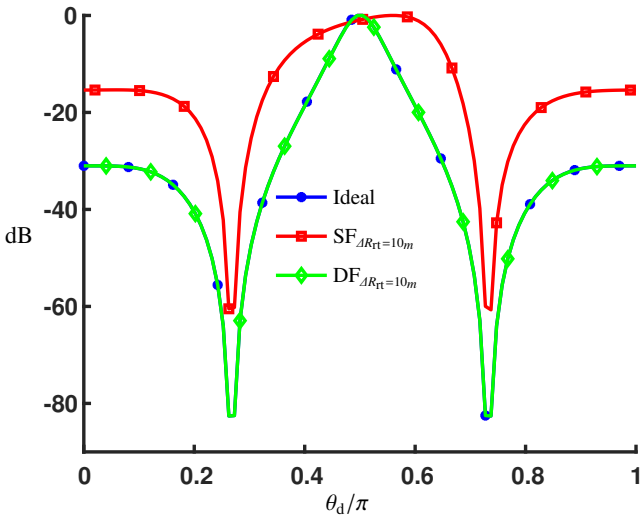

Figure 3.18: Simulating a 3 element ULA with $r_1 = 0.6^2$, $r_2 = 0.6$ (hence $\kappa = 0.6$), assuming an infinite SNR. For each target direction θ_d, the DF BF output Z_{DF} is evaluated where the beamformer is set to enhance signals impinging from $\theta_d = \pi/2$. The (modulus λ) range error is $\Delta R_{rt} = 0.3\lambda$. The SF BF (red squares) and the dual-frequency solution (green diamonds) are compared to the ideal response $\Delta R_{rt} = 0$ (blue dots) as a reference.

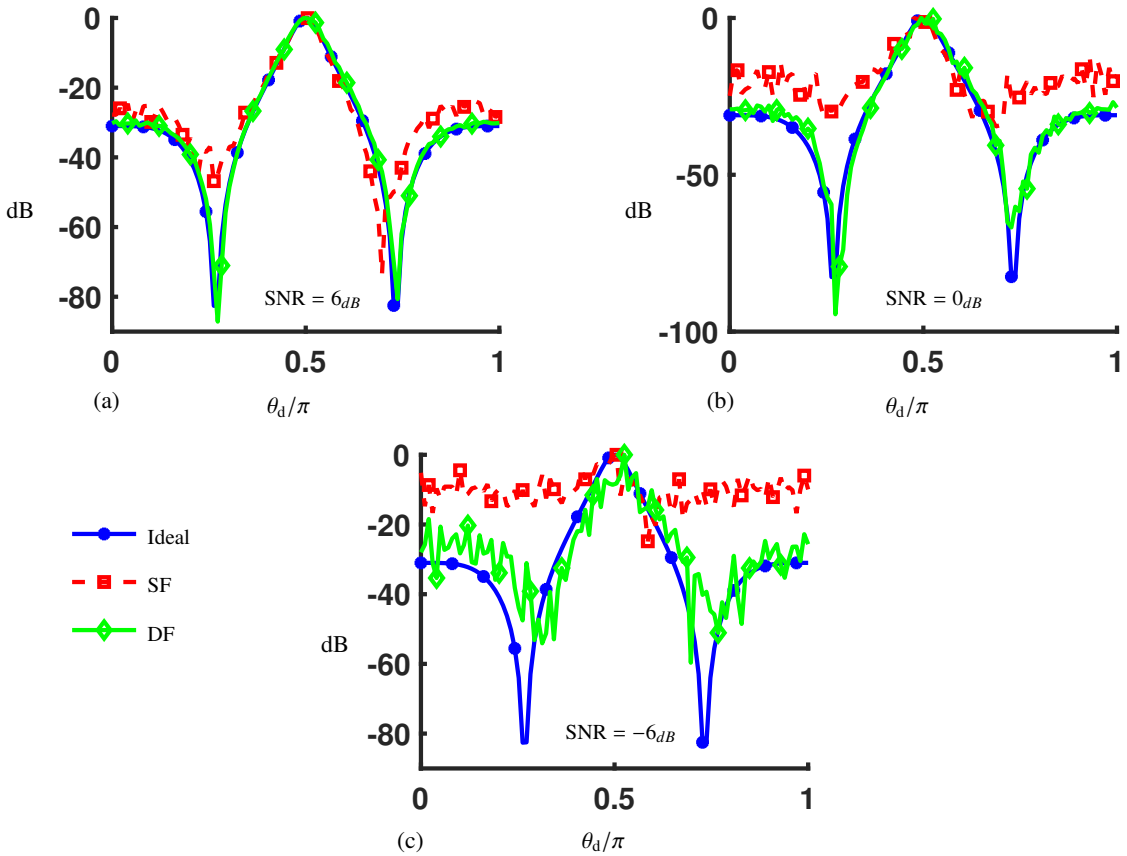

Figure 3.19: Directional response of the 3 element ULA, as in Fig. 3.18, simulated for the noisy scenario. The additive noises $n_1(t)$ and $n_2(t)$ (see Fig. 3.17), are set to obtain SNRs of 6 dB (a), 0 dB (b) and −6 dB (c).

Chapter 4

Conclusions

In this work we have suggested a novel approach to beamforming and localization, which is based on generating a continuous feedback between the array and the target of interest. Integrating feedback into standard beamformers proved to achieve the spatial domain equivalent of the temporal IIR filtering. It seems that a simple generalization of the conventional-beamformer maximizes (locally) the system's spatial information, thus enabling high localization accuracy. The feedback-based architecture performance evaluation predicts an unlimited improvement in all criteria, when considering perfect knowledge of the target's range and channel attenuation. It turns out that a single frequency waveform based feedback-beamformer is impractical, being too sensitive to even mild target range estimation errors. Fortunately, using a DF waveform and applying simple frequency domain manipulations to the output and feedback signals, was found to serve as a low frequency (hence low sensitivity) equivalent of the single frequency scheme. Also, the DF scheme proved to be of low noise sensitivity, featuring high performance even in relatively low signal-to-noise-ratio scenarios.

In the following, we overview some interesting leads for future study of the FB concept.

4.1 Future research

In the following chapter, some of the many possibilities for further investigation of the FB are suggested. As mentioned in Sec. 3.1, we assumed a single stationary target scenario where the target's location is fixed. Naturally, the first suggested subjects for future research are dynamic (Sec. 4.1.1) and multiple (Sec. 4.1.2) target scenarios. Another setting which may be an interesting subject for future research is the waveform characteristics (Sec. 4.1.3) and its effect on the overall spatial performance. We choose to conclude with another final suggestion (Sec. 4.1.4) - i.e. to revisit Sec.3.2's FIM related considerations to the choice of array settings.

4.1.1 Dynamic target

Revisiting (3.1), a natural initial generalization would be to allow the target of interest to be dynamic, i.e. introducing a general 3D arbitrary target location $\boldsymbol{p}_t(t)$. The location dynamics may be represented in terms of dynamic propagation delay, $\tau_{pd}(t)$ and Doppler.

Following the basic steps of temporal analysis, as in Chapter. 3, we start with expressing the impinging signal of a single sensor. As in the analysis of static target scenario, the signal consists of two contributions, i.e. the reflected emitted signal and the reflected feedback signal. Therefore, for each moment t, we should resolve the corresponding moment in which the current impinging signals were emitted by the array.

To this end, we first denote $t_{\text{ref}}(t)$ as the moment in which the currently impinging signal was reflected by the target of interest. Another auxiliary quantity is the reflection moment's corresponding target range $R(\tau_{\text{ref}})$ where the following relation holds

$$t - t_{\text{ref}}(t) = \frac{R(t_{\text{ref}}(t))}{c}. \tag{4.1}$$

Assuming $t_{\text{ref}}(t)$ is resolved, we denote the propagation delay at the reflection moment $\tau_{\text{ref}}(t) = R(t_{\text{ref}}(t))/c$ and express the emission moment as

$$t_{\text{TX}}(t) = t_{\text{ref}}(t) - \tau_{\text{ref}}(t) = t - 2\tau_{\text{ref}}(t). \tag{4.2}$$

With t_{TX}, we rewrite (3.1) as

$$x_n(t) = g\left(s(t_{\text{TX}}(t)) + \sum_{m=0}^{N-1} \alpha_m^* x_m(t_{\text{TX}}(t))\right). \tag{4.3}$$

Obviously, to have a closed form expression for $x_n(t)$, there should be a model for the target's dynamics (i.e. $\boldsymbol{p}_{\text{t}}$). Such an example, is a target with constant radial (constant DOA) velocity v with respect to the array which is initially positioned with distance of R_0 from the array, i.e.

$$R(t) = R_0 + vt. \tag{4.4}$$

Next, to resolve $t_{\text{ref}}(t)$, we plug (4.4) into (4.1) which results in

$$\begin{aligned} t - t_{\text{ref}}(t) &= \frac{R_0 + vt_{\text{ref}}}{c} \\ \Rightarrow t_{\text{ref}}(t) &= \frac{ct - R_0}{c + v}. \end{aligned} \tag{4.5}$$

Now, we express $\tau_{\text{ref}}(t)$ as

$$\begin{aligned} \tau_{\text{ref}}(t) &= t - t_{\text{ref}}(t) \\ &= \frac{R_0 + vt}{c + v}. \end{aligned} \tag{4.6}$$

which when plugged into (4.2) gives rise to

$$\begin{aligned} t_{\text{TX}}(t) &= t - 2\tau_{\text{ref}}(t) \\ &= \frac{c - v}{c + v} t - \frac{2R_0}{c + v} \end{aligned} \tag{4.7}$$

which when setting $v = 0$ degenerates to the static target scenario $t_{\mathrm{TX}}(t) = t - \frac{2R_0}{c}$. It follows that

$$x_n(t) = g\left[s\left(\frac{c-v}{c+v}t - \frac{2R_0}{c+v}\right) + \sum_{m=0}^{N-1} \alpha_m^* x_m\left(\frac{c-v}{c+v}t - \frac{2R_0}{c+v}\right)\right]. \tag{4.8}$$

Then, similar steps as in Sec. 3.1 are to be made to get an expression for the system's response H. It is expected that as in RADAR systems, the tracking of the object should now also take Doppler shifts into account.

4.1.2 Multi-target scenario

Considering practical scenarios of multiple (P) targets, positioned in $p_{t,i}$ $\forall i \in 0 \ldots P-1$, the obvious generalization of (3.1) is

$$x_n(t) = \sum_{i=0}^{P-1}\left[g\left(s\left(t - \tau_{pd,i} - \tau_{n,i}\right) + \sum_{m=0}^{N-1} \alpha_m^* x_m\left(t - \tau_{pd,i} - \tau_{n,i}\right)\right)\right], \tag{4.9}$$

where $\tau_{pd,i}$ is the delay of the signal which reflected from $p_{t,i}$. Interesting directions of research may include

- The effects of closely positioned targets
- Localization resolution
- Maximal number of simultaneously detected targets with respect to N
- Independent beamforming per target with multiple transmitters steering the feedback signal.

4.1.3 Waveform modifications

In modern RADAR related systems, the waveform of choice is pulse based and modulated by CW, or linear/nonlinear frequency scans. It holds some obvious advantages over the CW transmission such as

- Lower power consumption due to lower transmissions duty cycle.
- The use of wide band signals increases spatial resolution in the radial axis.

Another interesting option is using several (possibly many) independent harmonics as super positioned multiple dual frequency beamformers, which simultaneously scan a wide area with multiple resolutions. By merely selecting harmonic couples and filter coefficients, each harmonics pair is pointed to a specific area. It follows that with the expense of computational effort (without adding elements to the array), it seems possible that one may have simultaneous scan of the entire arena in any wanted direction/range/resolution.

As a simple example, consider that the arena consists of M zones of interest, where each zone may be described as a angular bounded radial slice (similar to the visualization of Fig. 3.2) which may be described as

$$a_m = \{\boldsymbol{p} \mid \theta_{d,m,\min} < \mathrm{DOA}\,(\boldsymbol{p}) < \theta_{d,m,\max}\ ,\ R_{m,\min} < \|\boldsymbol{p}\| < R_{m,\max}\}\ \forall\ m = 0 \ldots M-1.$$

Each zone will be assigned with matching couple of carrier frequencies ($\omega_{1,2}$) to cover its radial width (where the radial width is equivalent to R_{rt} of (3.25)) and coefficient sets ($\boldsymbol{\alpha}_{m,i}, \boldsymbol{\beta}_{m,i}\ \forall\ m = 0 \ldots M-1, i = 1,2$), which cover the zone's angular diameter which is equivalent to determining the desired beamwidth via setting the proper κ of (3.26).

Leaving aside the needed computational effort and physical limitations of transmitting multiple narrowband signals, assuming large M values, we have a super-positioned FB which simultaneously scans the entire arena.

4.1.4 Coefficients quality criteria

As mentioned in Sec. 3.1, the reasoning for the selection of $\boldsymbol{\alpha}, \boldsymbol{\beta}$ as the CB generalization, was the FIM related information considerations. Obviously, there are many more possibilities/considerations to choosing the coefficient. Some examples for such coefficient choosing schemes may include

- Finite word effects
- Nulling of specific DOAs
  For example, it is interesting to see the FB equivalent to Capon's [5] MVDR.

and many more.

Appendix A

Fisher Information Matrix

In the parameter estimation problems, we obtain information about the parameter from a sample of data coming from the underlying probability distribution. A natural question is: how much information can a sample of data provide about the unknown parameter? To this end, the FIM, which is the common tools for assessing the amount of available information in the sampled data is overviewed in the following.

Consider a random variable x for which the PDF is $f(x|\theta)$, where θ is an unknown parameter and $\theta \in \Theta$, with Θ is the parameter space. Intuitively, if an event has small probability, then the occurrence of this event brings us much information. For a random variable $X \sim f(x|\theta)$, if θ were the true value of the parameter, the likelihood function should take a big value, or equivalently, the derivative log-likelihood function should be close to zero, and this is the basic principle of maximum likelihood estimation. We define $l(x|\theta) = \log f(x|\theta)$ as the log-likelihood function which follows that the Fisher information may be expressed [34] as

$$I(\theta) = -E_\theta \{l''(x|\theta)\} = -\int \left[\frac{\partial^2}{\partial \theta^2} \log f(x|\theta) f(x|\theta) \right] dx \tag{A.1}$$

.

A.0.1 Cramér-Rao Lower Bound and Asymptotic Distribution of Maximum Likelihood Estimators

In practical applications, where signal is noisy and parameters cannot be accurately estimated, having a closed form expression for the FIM naturally leads to seek for a performance bound that will help the user to know when available information is fully utilized. Such a bound for unbiased estimators is [34]

$$\mathrm{Var}_\theta \left\{ \hat{\theta} \right\} \geq I^{-1}(\theta).$$

The right hand side is the CRLB: under certain conditions, no other unbiased estimator of the parameter θ can have a variance smaller than CRLB.

A.0.2 The Multiple Parameter Case

Suppose now there are more than one parameter in the distribution model, that is, the random variable $X \sim f(x|\boldsymbol{\theta})$ with $\boldsymbol{\theta} = (\theta_0, ;\theta_{k-1})^T$. We denote the log-likelihood function as

$$l(\boldsymbol{\theta}) = \log f(x|\boldsymbol{\theta}),$$

and its first order derivative with respect to $\boldsymbol{\theta}$ is a k-dimensional vector, which is

$$\frac{\partial l(\boldsymbol{\theta})}{\partial \boldsymbol{\theta}} = \left(\frac{\partial l(\boldsymbol{\theta})}{\partial \theta_0}, \ldots, \frac{\partial l(\boldsymbol{\theta})}{\partial \theta_{k-1}} \right)^T,$$

The second order derivative of $l(\boldsymbol{\theta})$ with respect to $\boldsymbol{\theta}$ is a $k \times k$ matrix, which is

$$\frac{\partial^2 l(\boldsymbol{\theta})}{\partial \boldsymbol{\theta}^2} = \left\{ \frac{\partial^2 l(\boldsymbol{\theta})}{\partial \theta_i \partial \theta_j} \right\}_{i,j \in [0,\ldots,k-1]}.$$

We define the *Fisher information matrix* as

$$I(\boldsymbol{\theta}) = E\left\{ \frac{\partial l(\boldsymbol{\theta})}{\partial \boldsymbol{\theta}} \left(\frac{\partial l(\boldsymbol{\theta})}{\partial \boldsymbol{\theta}} \right)^T \right\} = \mathrm{Cov}\left\{ \frac{\partial l(\boldsymbol{\theta})}{\partial \boldsymbol{\theta}} \right\} = -E\left\{ \frac{\partial^2 l(\boldsymbol{\theta})}{\partial \boldsymbol{\theta}^2} \right\}.$$

Since the covariance matrix is symmetric and semi-positive definite, these properties hold for the Fisher information matrix as well.

A.0.3 FIM applications

Considering unbiased estimators, the CRLB for the multi-parameter case can be shown to be

$$\mathrm{Cov}_{\boldsymbol{\theta}}\left\{ \hat{\boldsymbol{\theta}}(\boldsymbol{X}) \right\} \geq I^{-1}(\boldsymbol{\theta}) \tag{A.2}$$

where the matrix inequality $A \geq B$ means that $A - B$ is positive semi-definite. From (A.2), it is obvious that when I'th determinant is increased, the CRLB decreases which implicates that the data is more informative and though not necessarily obtainable, an optimal estimator will achieve higher accuracy in such scenario.

A.0.4 Frequency Domain Cramér-Rao Bound for Gaussian Processes

The interesting work of [42] (which also specifically states its contribution to localization applications) enables the generalization of the CRLB to the frequency domain, which is of high relevance to this work (see Sec.3.2). Assuming Gaussian processes, the results of [40] are

utilized together with further development to find that

$$
\begin{aligned}
J_{k,l}(\boldsymbol{\eta}) = & \frac{1}{2\pi}\int_{-\omega_s/2}^{\omega_s/2}\frac{1}{\Phi(\omega)}\mathfrak{F}^*\left\{\frac{\partial z(t)}{\partial \eta_k}\right\}\mathfrak{F}\left\{\frac{\partial z(t)}{\partial \eta_l}\right\}d\omega \\
& + \frac{T}{4\pi}\int_{-\omega_s/2}^{\omega_s/2}\frac{1}{\Phi^2(\omega)}\left(\frac{\partial \Phi(\omega)}{\partial \eta_k}\right)^*\frac{\partial \Phi(\omega)}{\partial \eta_l}d\omega
\end{aligned}
\tag{A.3}
$$

which is conveniently generalized to the complex data case used in this work as (3.4).

Appendix B

FIM calculation

Following (3.5), we elaborate the steps leading to (3.7). First, we express the partial derivatives of Z with respect to $\boldsymbol{\eta}$, resulting in

$$\begin{aligned}
\frac{1}{\mathrm{S}}\frac{\partial \mathrm{Z}}{\partial \theta_{\mathrm{d}}} &= \frac{g\boldsymbol{\beta}^H \boldsymbol{A}\boldsymbol{d}\exp(-j\phi)\left(1-g\boldsymbol{\alpha}^H\boldsymbol{d}\exp(-j\phi)\right)+g^2\boldsymbol{\beta}^H\boldsymbol{d}\boldsymbol{\alpha}^H\boldsymbol{A}\boldsymbol{d}\exp(-2j\phi)}{\left(1-g\boldsymbol{\alpha}^H\boldsymbol{d}\exp(-j\phi)\right)^2} \\
&= \frac{g\boldsymbol{\beta}^H \boldsymbol{A}\boldsymbol{d}\exp(-j\phi)-g^2\boldsymbol{\beta}^H\left(\boldsymbol{A}\boldsymbol{d}\boldsymbol{d}^T-\boldsymbol{d}\boldsymbol{d}^T\boldsymbol{A}\right)\boldsymbol{\alpha}^*\exp(-2j\phi)}{\left(1-g\boldsymbol{\alpha}^H\boldsymbol{d}\exp(-j\phi)\right)^2} \\
&= \frac{g\boldsymbol{\beta}^H \boldsymbol{A}\boldsymbol{d}\exp(-j\phi)+g^2\boldsymbol{\beta}^H\boldsymbol{B}\boldsymbol{\alpha}^*\exp(-2j\phi)}{\left(1-g\boldsymbol{\alpha}^H\boldsymbol{d}\exp(-j\phi)\right)^2}
\end{aligned}$$

and

$$\begin{aligned}
\frac{1}{\mathrm{S}}\frac{\partial \mathrm{Z}}{\partial \phi} &= \frac{-jg\boldsymbol{\beta}^H\boldsymbol{d}\exp(-j\phi)\left(1-g\boldsymbol{\alpha}^H\boldsymbol{d}\exp(-j\phi)\right)-jg^2\boldsymbol{\beta}^H\boldsymbol{d}\boldsymbol{\alpha}^H\boldsymbol{d}\exp(-2j\phi)}{\left(1-g\boldsymbol{\alpha}^H\boldsymbol{d}\exp(-j\phi)\right)^2} \\
&= \frac{-jg\boldsymbol{\beta}^H\boldsymbol{d}\exp(-j\phi)}{\left(1-g\boldsymbol{\alpha}^H\boldsymbol{d}\exp(-j\phi)\right)^2}
\end{aligned},$$

where we defined $\boldsymbol{B} \triangleq \boldsymbol{d}\boldsymbol{d}^T\boldsymbol{A}-\boldsymbol{A}\boldsymbol{d}\boldsymbol{d}^T$. The main diagonal elements of the FIM are

$$\begin{aligned}
J_{\theta_{\mathrm{d}}\theta_{\mathrm{d}}} &= \Re\left\{\frac{1}{2\pi\sigma^2}\int_{-\omega_s/2}^{\omega_s/2}\left|\frac{\partial \mathrm{Z}}{\partial \theta_{\mathrm{d}}}\right|^2 d\omega\right\} \\
&= \frac{1}{2\pi\sigma^2}\int_{-\omega_s/2}^{\omega_s/2}\frac{\left|g\boldsymbol{\beta}^H\boldsymbol{A}\boldsymbol{d}-g^2\boldsymbol{\beta}^H\boldsymbol{B}\boldsymbol{\alpha}^*\exp(-j\phi)\right|^2}{\left|1-g\boldsymbol{\alpha}^H\boldsymbol{d}\exp(-j\phi)\right|^4}|\mathrm{S}|^2\,d\omega, \\
J_{\phi\phi} &= \Re\left\{\frac{1}{2\pi\sigma^2}\int_{-\omega_s/2}^{\omega_s/2}\left|\frac{\partial \mathrm{Z}}{\partial \phi}\right|^2 d\omega\right\} \\
&= \frac{1}{2\pi\sigma^2}\int_{-\omega_s/2}^{\omega_s/2}\frac{\left|g\boldsymbol{\beta}^H\boldsymbol{d}\right|^2}{\left|1-g\boldsymbol{\alpha}^H\boldsymbol{d}\exp(-j\phi)\right|^4}|\mathrm{S}|^2\,d\omega
\end{aligned}$$

and the cross terms are

$$
\begin{aligned}
&J_{\theta_{\mathrm{d}}\phi} = J^*_{\phi\theta_{\mathrm{d}}} = \\
&= \Re\left\{\frac{1}{2\pi\sigma^2}\int_{-\omega_s/2}^{\omega_s/2}\left(\frac{\partial \mathrm{Z}}{\partial\phi}\right)^*\frac{\partial \mathrm{Z}}{\partial\theta_{\mathrm{d}}}d\omega\right\} \\
&= \Re\left\{\frac{1}{2\pi\sigma^2}\int_{-\omega_s/2}^{\omega_s/2}\frac{jg^2\boldsymbol{\beta}^T\boldsymbol{d}^*\boldsymbol{\beta}^H\left(\boldsymbol{A}\boldsymbol{d}+g\boldsymbol{B}\boldsymbol{\alpha}^*\exp\left(-j\phi\right)\right)}{\left|1-g\boldsymbol{\alpha}^H\boldsymbol{d}\exp\left(-j\phi\right)\right|^4}\left|\mathrm{S}\right|^2 d\omega\right\}.
\end{aligned}
$$

Notice that when the weights are proportional to the conjugated steering vector, i.e.,

$$\boldsymbol{\alpha},\boldsymbol{\beta}\propto\boldsymbol{d}^*,$$

the $\boldsymbol{\beta}^T B\boldsymbol{\alpha}$ term vanishes. Assuming a real input waveform $s(t)$, the function

$$\frac{\left|\mathrm{S}\right|^2}{\left|1-g\boldsymbol{\alpha}^H\boldsymbol{d}\exp\left(-j\phi\right)\right|^4}$$

is even with respect to ω, and

$$\boldsymbol{\beta}^H\boldsymbol{A}\boldsymbol{d}\propto\boldsymbol{d}^H\boldsymbol{A}\boldsymbol{d}=\sum_{n=0}^{N-1}A_{n,n}\left|\boldsymbol{d}_n\right|^2\propto\omega$$

is odd, hence the cross terms vanish.

Appendix C

Half power beamwidth

We now compute the squared norm of (3.14), equate it to $1/2$ and compute the value of $N\Delta\theta/2$ for large N. To this end, we denote $\gamma \triangleq \Delta\theta/2$, giving rise to

$$\begin{aligned}\left|\mathcal{H}_{\Delta\theta,\Delta\phi=0,r}(\omega)\right|^2 &= \frac{(1-r)^2\,\mathrm{D}^2(\gamma,N)}{\left|\exp\left(j(N-1)\gamma\right)-r\mathrm{D}(\gamma,N)\right|^2} \\ &\overset{N\gg 1}{\approx} \frac{(1-r)^2\,\mathrm{D}^2(\gamma,N)}{1-2r\cos(N\gamma)\mathrm{D}(\gamma,N)+r^2\mathrm{D}^2(\gamma,N)}.\end{aligned}$$

Equating to $1/2$, leads to

$$\left(r^2-4r+2\right)\mathrm{D}^2(\gamma,N)+2r\cos(N\gamma)\mathrm{D}(\gamma,N)-1=0.$$

Since for large N, the mainlobe beamwidth goes to zero, we approximate $\sin(\gamma)$ with γ. Also defining $x \triangleq N\gamma = N\Delta\theta/2$ we obtain (3.15).

Appendix D

Fitting the array's directivity

In the process of simplifying (3.19) in order to find the expression for the directivity $\mathcal{D}$, we noticed the results were a rational expression. Following this observation, we numerically swept various values of N, r pairs, trying find a common expression that fits all results which will enable the formulation of the directivity improvement when using the FB. In the following, we elaborate on the technicalities of this sweeping process.

The first step was to formulate the symbolic expression for H. To this end, we used MATLAB®'s symbolic toolbox, generating the symbolic response H. Afterwards, the 2D sweep range was set, where as mentioned before, r was set to be of rational values. In each sweep step, a numerical integration was executed with specific values for N and r. Each result was fitted with it's next closest rational number with the help of MATLAB®'s *rats* auxiliary command. After observing the results, we found that all of them obey the same expression as in (3.20) for any tolerance, which increased the confidence in the suggested expression.

The printout of the code is presented as Table. D.1 and the text below.

Table D.1: Performances of Classical ULA and the Proposed Feedback-Beamforming Architecture, with a Gain Mismatch r.

$r\backslash N$	2	3	4	5	6	7	8	9	10
1/10	19/9	29/9	13/3	49/9	59/9	23/3	79/9	89/9	11
1/5	9/4	7/2	19/4	6	29/4	17/2	39/4	11	49/4
1/3	5/2	4	11/2	7	17/2	10	23/2	13	29/2
1/2	3	5	7	9	11	13	15	17	19
5/8	11/3	19/3	9	35/3	43/3	17	59/3	67/3	25
3/4	5	9	13	17	21	25	29	33	37
4/5	6	11	16	21	26	31	36	41	46

MATLAB® Code

```
function [] = directivityAnalysis()
%% configure
nVec     = 2:10;
rVec     = [1/10 1/5 1/3 1/2 5/8 3/4 4/5];

%% symbolics
syms x real;
syms r positive;

D = @(x,N) sin(N*x)/(N*sin(x));

hNum = @(t,p,N,r) (1-r)*D(t/2,N);
hDen = @(t,p,N,r) exp(1i*(p+(N-1)*t/2)) - r*D(t/2,N);
h = @(t,p,N,r) hNum(t,p,N,r)./hDen(t,p,N,r);

%% simulate
integralResultMAT   = zeros(length(rVec),length(nVec));
exprMAT             = zeros(size(integralResultMAT));
[r_GRID, n_GRID]    = meshgrid(rVec, nVec);
for rVal = rVec
    for nVal = nVec
        curIntRes = ...
            vpaintegral(h(x,0,nVal,rVal), 0, 2*pi...
            ) ...
            /(2*pi);
        Dir = 1 / curIntRes;
        curIntRes_eval = eval(curIntRes);
        curIntRes_STR = num2str(real(curIntRes_eval));
        Dir_eval = eval(Dir);
        Dir_STR = rats(real(Dir_eval));
        tol = abs(eval(Dir_STR)-Dir_eval);
        disp([...
            'r = ', num2str(rVal) ...
            ,', N = ', num2str(nVal) ...
            ,', int = ',  curIntRes_STR ...
            ,', Dir = ', Dir_STR ...
            ]);
        integralResultMAT(...
            rVec == rVal,...
            nVec == nVal...
            ) = real(Dir_eval);
        exprMAT(...
            rVec == rVal,...
            nVec == nVal...
            ) = (nVal-rVal)/(1-rVal);
    end
end
figure;
```

```
surf(r_GRID, n_GRID, transpose(integralResultMAT), 'EdgeColor', ...
    "interp", 'FaceAlpha',0.75);
hold on;
plot3(r_GRID, n_GRID, transpose(exprMAT), 'dk', 'MarkerSize', 10, ...
    'LineWidth', 2, 'MarkerFaceColor', 'k');
legend({'Numeric integration', 'Analytic expression'});
```

Appendix E

Proof of Theorem 3.1

Proof. Elaborating (3.22) gives rise to

$$
\begin{aligned}
Z_{\mathrm{DF}}^{-1} &= \left| \frac{1 - g_1 \boldsymbol{\alpha}_1^H \boldsymbol{d}_1 e^{-j\phi_1}}{g_1 \boldsymbol{\beta}_1^H \boldsymbol{d}_1 e^{-j\phi_1}} + \frac{1 - g_2 \boldsymbol{\alpha}_2^H \boldsymbol{d}_2 e^{-j\phi_2}}{g_2 \boldsymbol{\beta}_2^T \boldsymbol{d}_2 e^{-j\phi_2}} \right| \\
&= \left| \frac{g_2 \boldsymbol{\beta}_2^H \boldsymbol{d}_2 e^{-j\phi_2} - g_1 g_2 \left(\boldsymbol{\alpha}_1^H \boldsymbol{d}_1 \boldsymbol{\beta}_2^H \boldsymbol{d}_2 + \boldsymbol{\alpha}_2^H \boldsymbol{d}_2 \boldsymbol{\beta}_1^H \boldsymbol{d}_1 \right) e^{-j(\phi_1+\phi_2)} + g_1 \boldsymbol{\beta}_1^H \boldsymbol{d}_1 e^{-j\phi_1}}{g_1 \boldsymbol{\beta}_1^H \boldsymbol{d}_1 g_2 \boldsymbol{\beta}_2^H \boldsymbol{d}_2} \right| \\
&= \left| \frac{g_2 \boldsymbol{\beta}_2^H \boldsymbol{d}_2 e^{j(\phi_1-\phi_2)} + g_1 \boldsymbol{\beta}_1^H \boldsymbol{d}_1}{g_1 \boldsymbol{\beta}_1^H \boldsymbol{d}_1 g_2 \boldsymbol{\beta}_2^H \boldsymbol{d}_2} - \frac{\left(\boldsymbol{\beta}_1^H \boldsymbol{d}_1 \boldsymbol{\alpha}_2^H \boldsymbol{d}_2 + \boldsymbol{\beta}_2^H \boldsymbol{d}_2 \boldsymbol{\alpha}_1^H \boldsymbol{d}_1 \right) e^{-j\phi_2}}{\boldsymbol{\beta}_1^H \boldsymbol{d}_1 \boldsymbol{\beta}_2^H \boldsymbol{d}_2} \right| .
\end{aligned}
$$

Note that in the special case of choosing $\boldsymbol{\alpha}_1 = \boldsymbol{\beta}_1$, $\boldsymbol{\alpha}_2 = -\boldsymbol{\beta}_2$, the resultant beampattern simplifies to

$$
Z_{\mathrm{DF}} = \left| \frac{g_1 \boldsymbol{\beta}_1^H \boldsymbol{d}_1}{1 + \frac{g_1 \boldsymbol{\beta}_1^H \boldsymbol{d}_1}{g_2 \boldsymbol{\beta}_2^H \boldsymbol{d}_2} \exp\left(-j\left(\phi_1 - \phi_2\right)\right)} \right| .
$$

Also setting $\boldsymbol{\beta}_2 = [-1/\hat{g}_2, 0, \ldots, 0]$ results in (3.24). ■

Bibliography

[1] JG Ables. Maximum entropy spectral analysis. *Astronomy and Astrophysics Supplement Series*, 15:383, 1974.

[2] Les Barclay. *Propagation of radiowaves*, volume 2. IET, 2003.

[3] J. Benesty, I. Cohen, and J. Chen. *Fundamentals of Signal Enhancement and Array Signal Processing*. Wiley-IEEE Press, Singapore, 2018.

[4] L Bruton and N Bartley. Three-dimensional image processing using the concept of network resonance. *IEEE Transactions on Circuits and Systems*, 32(7):664–672, 1985.

[5] Jack Capon. High-resolution frequency-wavenumber spectrum analysis. *Proceedings of the IEEE*, 57(8):1408–1418, 1969.

[6] Pascal Chevalier, Laurent Albera, Anne Ferréol, and Pierre Comon. On the virtual array concept for higher order array processing. *IEEE Transactions on Signal Processing*, 53(4):1254–1271, Apr 2005.

[7] Pascal Chevalier, Anne Ferréol, and Laurent Albera. High-resolution direction finding from higher order statistics: The 2^q-music algorithm. *IEEE Transactions on signal processing*, 54(8):2986–2997, 2006.

[8] Pierre Comon. Independent component analysis, a new concept? *Signal processing*, 36(3):287–314, 1994.

[9] Mithat C Dogan and Jerry M Mendel. Applications of cumulants to array processing. i. aperture extension and array calibration. *IEEE Transactions on Signal Processing*, 43(5):1200–1216, May 1995.

[10] Otis Lamont Frost. An algorithm for linearly constrained adaptive array processing. *Proceedings of the IEEE*, 60(8):926–935, 1972.

[11] S V Hum, H L P A Madanayake, and L T Bruton. Beamforming using 2-D Digital Filters. 57(3):804–807, 2009.

[12] Aapo Hyvärinen. Survey on independent component analysis. 1999.

[13] Hamid Krim and Mats Viberg. Two decades of array signal processing research: the parametric approach. *IEEE signal processing magazine*, 13(4):67–94, 1996.

[14] E. Kupershtein, M. Wax, and I. Cohen. Single-site emitter localization via multipath fingerprinting. *IEEE Trans. Signal Processing*, 61(1):10–21, Jan 2013.

[15] T. Long, J. Chen, G. Huang, J. Benesty, and I. Cohen. Acoustic source localization based on geometric projection in reverberant and noisy environments. *Special Issue of the IEEE Journal of Selected Topics in Signal Processing on Acoustic Source Localization and Tracking in Dynamic Real-life Scenes*, 13(1):482–495, Mar 2019.

[16] Verne H MacDonald and Peter M Schultheiss. Optimum passive bearing estimation in a spatially incoherent noise environment. *The Journal of the Acoustical Society of America*, 46(1A):37–43, 1969.

[17] HLP Arjuna Madanayake and Leonard T Bruton. A speed-optimized systolic array processor architecture for spatio-temporal 2D IIR broadband beam filters. *IEEE Transactions on Circuits and Systems I: Regular Papers*, 55(7):1953–1966, 2008.

[18] Dimitris G Manolakis, Vinay K Ingle, Stephen M Kogon, et al. *Statistical and adaptive signal processing: spectral estimation, signal modeling, adaptive filtering, and array processing*. McGraw-Hill Boston, 2000.

[19] Alan Moffet. Minimum-redundancy linear arrays. *IEEE Transactions on antennas and propagation*, 16(2):172–175, Mar 1968.

[20] Or Nadiri and Boaz Rafaely. Localization of multiple speakers under high reverberation using a spherical microphone array and the direct-path dominance test. *IEEE/ACM Transactions on Audio, Speech, and Language Processing*, 22(10):1494–1505, 2014.

[21] Alan V Oppenheim and Ronald W Schafer. *Digital signal processing*. Prentice-Hall, 1975.

[22] Piya Pal and PP Vaidyanathan. Nested arrays: A novel approach to array processing with enhanced degrees of freedom. *IEEE Transactions on Signal Processing*, 58(8):4167–4181, Aug 2010.

[23] S Pillai and Fred Haber. Statistical analysis of a high resolution spatial spectrum estimator utilizing an augmented covariance matrix. *IEEE Transactions on Acoustics, Speech, and Signal Processing*, 35(11):1517–1523, Aug 1987.

[24] S Unnikrishna Pillai, Yeheskel Bar-Ness, and Fred Haber. A new approach to array geometry for improved spatial spectrum estimation. *Proceedings of the IEEE*, 73(10):1522–1524, 1985.

[25] LR Rabiner, JF Kaiser, O Herrmann, and MT Dolan. Some comparisons between fir and iir digital filters. *Bell System Technical Journal*, 53(2):305–331, 1974.

[26] R. Roy and T. Kailath. Esprit-estimation of signal parameters via rotational invariance techniques. *IEEE Transactions on Acoustics, Speech, and Signal Processing*, 37(7):984–995, 1989.

[27] Ralph Schmidt. Multiple emitter location and signal parameter estimation. *IEEE transactions on antennas and propagation*, 34(3):276–280, Mar 1986.

[28] Fe Schweppe. Sensor-array data processing for multiple-signal sources. *IEEE Transactions on Information Theory*, 14(2):294–305, 1968.

[29] Ali Shareef, Yifeng Zhu, and Mohamad Musavi. Localization using neural networks in wireless sensor networks. In *Proceedings of the 1st international conference on MOBILe Wireless MiddleWARE, Operating Systems, and Applications*, pages 1–7, 2008.

[30] Jack Sherman and Winifred J Morrison. Adjustment of an inverse matrix corresponding to a change in one element of a given matrix. *The Annals of Mathematical Statistics*, 21(1):124–127, 1950.

[31] M.I. Skolnik. *Radar Handbook, Third Edition*. Electronics electrical engineering. McGraw-Hill Education, 2008.

[32] Petre Stoica and Arye Nehorai. MUSIC, maximum likelihood, and Cramer-Rao bound. *IEEE Transactions on Acoustics, speech, and signal processing*, 37(5):720–741, 1989.

[33] T Engin Tuncer and Benjamin Friedlander. *Classical and modern direction-of-arrival estimation*. Academic Press, 2009.

[34] Harry L Van Trees. *Detection, estimation, and modulation theory, part I: detection, estimation, and linear modulation theory*. John Wiley & Sons, 2004.

[35] Harry L Van Trees. *Optimum array processing: Part IV of detection, estimation, and modulation theory*. John Wiley & Sons, 2004.

[36] Barry D Van Veen and Kevin M Buckley. Beamforming: A versatile approach to spatial filtering. *IEEE ASSP magazine*, 5(2):4–24, Apr 1988.

[37] Sergio Verdu et al. *Multiuser detection*. Cambridge university press, 1998.

[38] Fuxi Wen, Boon Poh Ng, and Vinod Veera Reddy. Extending the concept of IIR filtering to array processing using approximate spatial IIR structure. *Multidimensional Systems and Signal Processing*, 24(1):157–179, Oct 2013.

[39] Geyi Wen. *Foundations for radio frequency engineering*. World Scientific, 2015.

[40] Peter Whittle. The analysis of multiple stationary time series. *Journal of the Royal Statistical Society: Series B (Methodological)*, 15(1):125–139, 1953.

[41] Max A Woodbury. Inverting modified matrices. *Memorandum report*, 42(106):336, Jun 1950.

[42] Ariela Zeira and Arye Nehorai. Frequency domain Cramer-Rao bound for Gaussian processes. *IEEE transactions on acoustics, speech, and signal processing*, 38(6):1063–1066, Jun 1990.

[43] W. Zeng, H. C. So, and L. Huang. ℓ_p-music: Robust direction-of-arrival estimator for impulsive noise environments. *IEEE Transactions on Signal Processing*, 61(17):4296–4308, 2013.

במהלך סקר הספרות, התגלה כי שאלה זו התעוררה גם במוחם של חוקרים אחרים. בעבודתו של WEN [38] הוצעו שתי שיטות. האחת מערבת שיערוך של כיוון הגעת הגל ויצירה מלאכותית של משוב. שיטה זו רגישה לשגיאות שיערוך ומעבר לכך, מערבת עיבוד זמני ולכן אינה מתאימה כתשובה לשאלת המחקר. השיטה השניה שהוצעה היתה הגדרת תתי מערכים (חלקים חופפים מהמערך המקורי) כך שאל מוצא כל תת מערך מתייחסים כאל הסחה זמנית של פלט מערך ייחוס כלשהו. ניתוח מתמטי מוכיח כי בפועל העיבוד המרחבי לא משתפר היות ובפועל מדובר במערך בעל מספר זהה של דרגות חופש ל FIR.

גישה נוספת, אשר מקורה בעיבוד אותות וידאו [4] , מתייחסת לכיוון ההגעה כאל תדר נוסף. במישור הדו תדרי (משמע התדר המרחבי והתדר הזמני) גל מישורי מיוצג ע"י קו ישר המוטה בהתאם לזוית הגעתו אל המערך. אי לכך, על מנת להגביר אותות מכיוונים רצויים, יש לתכנן מסננים המעבירים פסים ישרים במישור הדו תדרי התואמים לכיווני הגעה אלו. היות ותגובת המסננים מחזורית בשני התדרים, נוצרים עיוותים בקצוות התגובה התדרית ובנוסף לכך, גם שיטה זו מערבת עיבוד זמני ולכן אינה מהווה פתרון מספק לשאלת המחקר.

כאמור, בעבודה זו מוצג לראשונה עקרון המסנן המשלב משוב מרחבי. בעזרת שילוב משדר במערך, משודרת חזרה לזירה גרסה מעובדת של האות הנקלט. היות ומניחים שהמטרה מחזירה את האותות המגיעים אליה, השידור בפועל אינו רק של האות הנקלט אלא כולל גם את הדי האותות שנקלטו בעבר ובכך נוצר חוג סגור בו המידע המרחבי נאסף בהדרגה בכל פעם שהאות חוזר. מניתוח המערך עולה כי בשילוב המשוב, תגובתו הינה המקבילה המרחבית למסנן בעל התגובה הזמנית האינסופית. בנוסף, עולה כי התגובה אינה מושפעת רק מכיוון הגעת הגל כמו במסננים המוכרים, אלא גם ממרחק המטרה מהמערך.

בשלב זה, על מנת לקבוע את משקלות המערך, הוגדרו המרחק וכיוון ההגעה כערכים אותם יש לשערך ובהתאם לכך חושבה מטריצת אינפורמציית פישר (FIM). בעזרת מטריצה זו נמצאו המקדמים המביאים את האינפורמציה לכדי שיא - בדיעבד, הרחבה טבעית של מקדמי האיסוף הקוהרנטי הבסיסי המוכר בספרות כמסנן הקונבנציונאלי. מסנן זה מסיח את הפאזה של האותות המגיעים מחיישנים שונים כך שאות המגיע מכיוון כלשהו יאסף בהתאבכות בונה.

ביצועי המערך מנותחים בהקשר של אפליקצית איכון וכוללים ניתוח של רוחב האונה המרכזית, הנחתת אונות הצד וכיווניות המערך. לשם ניתוח זה נעשה שימוש בכלים מהספרות הקלאסית על מנת לאפשר השוואה אובייקטיבית אל המערכים המקובלים ללא המשוב. כידוע, ביצועי המערך קשורים קשר ישיר למפתח הפיזי שלו. אי לכך, לשם המחשת התוצאות, השיפור בביצועי המערך מוצג כהגדלה וירטואלית של מפתח המערך. בנוסף, הניתוח מראה כי ניתן ליישם את עקרון המשוב בכל מערך ולא רק ב ULA.

סימולציות בשילוב בחינה דקדקנית של המערכת מגלים כי המערכת בעלת רגישות גבוהה למדי לשגיאת טווח. היות ושגיאה זו שקולה לאורך הגל לפיו פועל המערך, הוצע שימוש בלתי תלוי בשני תדרים קרובים תוך נסיון לחלץ את המידע המרחבי מהקשר בין האותות הנקלטים. הפתרון פשוט וזול יחסית ומגדיל בסך הכל את המאמץ החישובי ולא את המערך עצמו. ניתוח נוסף מאשרר כי הפתרון קביל ומשיג תוצאות שבתרחישים אידיאלים נוטות לכדי שיפור משמעותי בביצועים המרחביים.

תקציר

בעבודה זו מוצגת שיטה חדשנית לעיבוד מרחבי של אותות במערכי חיישנים. בבסיס השיטה נעשה שימוש במשוב מרחבי הניזון מהאותות הנקלטים במערך כך שלא מתבצע עיבוד זמני על האות הנקלט כי אם עיבוד מרחבי בלבד. מניתוח ביצועי המערך עולה שיפור ניכר ביחס למערכים הידועים. לשם נוחות, העבודה מוצגת בהקשר של איכון אך ניתנת להרחבה למגוון רחב של אפליקציות המשלבות עיבוד מרחבי של אותות ע"י מערכי חיישנים.

עיבוד מערכי חיישנים הינו תחום מחקר ענף הנותן מענה למגוון רחב של בעיות ועדויות מוקדמות לשימוש בו ניתן למצוא עוד בתקופת מלחמת העולם השניה בדמות רדאר ה Mammut שנבנה על ידי הגרמנים לזיהוי מוקדם של מטרות טסות בגבהים עד 8 ק"מ ומרחקים של עד 300 ק"מ. במערכות תקשורת לדוגמא, הצורך בסינון מרחבי הוא מן המעלה הראשונה לאור המציאות מרובת המשדרים והמקלטים. בנוסף, הכוונת אלומת השידור מתאפשרת בזכות השימוש במערכי מופע (phased array) ובכך מושגים חסכון באנרגית שידור, מניעת הגעת המידע ליעדים בלתי רצויים, חסינות לרעשים ועוד. בדימות רפואית כדוגמת CT, MRI, EEG וכו', רופאים מייצרים מודלים של פנים גוף האדם באופן בלתי פולשני ע"י שימוש בעיבוד מרחבי מבוסס מערכי חיישנים. בטלפונים הניידים מצויים מערכי מיקרופונים אשר מסננים את אות הדובר על פי כיוון הגעתו ומאפייניו הסטטיסטיים. בתחום האסטרונומיה, מערכי אנטנות רדיו הנפרשים על פני שטחים עצומים משמשים הלכה למעשה טלסקופים רבי עוצמה ודיוק. ככלל, בין תחומי מחקר אלו, מתקיימת תרומה הדדית רחבת היקף, כך שמסקנות העולות מתחום כלשהו לעיתים קרובות משמשות בסיס למחקר ופיתוח בתחומים אחרים.

המערך היוניפורמי הלינארי (ULA) בו החיישנים מפוזרים על קו ישר במרחקים קבועים האחד מהשני נחשב למערך הבסיסי בעיבוד המרחבי בשל פשטות העיבוד והניתוח האנליטי שלו. בנוסף, מוכרת בספרות ההקבלה בין עיצוב אלומת הסריקה (בהקשר של איכון) של מערך זה לבין תכן מסננים בעלי תגובה סופית להלם (FIR). הקבלה זו נובעת בין היתר מכך שבהינתן כיוון הגעת חזית הגל, הפרש הזמן בין הגעתה מחיישן אחד לשכנו זהה להפרש זמני ההגעה מהחיישן השכן אל הבא אחריו. תכונה זו מאפשרת הקבלה בין הפרשי זמני ההגעה לבין יחידות ההשהיה המשמשות למימוש המסננים הזמניים. בנוסף, לאחר ניתוח מתמטי, ניתן לראות הקבלה בין כיוון הגעת חזית הגל בעיבוד המרחבי לבין התדר הזמני בעיבוד הזמני, לכן כיוון הגעת הגל נחשבת לתדר המרחבי.

קיימת ארכיטקטורה נוספת למסננים, הממשת מסנן בעל תגובה אינסופית להלם (IIR) ע"י שילוב היזון חוזר. מסננים אלו מאופיינים ביעילות מוגברת, כלומר עבור דרישות זהות בתגובת התדר, למסנן ה IIR ידרשו פחות מקדמים. יתרון זה מהווה כבסיס לשאלת המחקר בתזה זו שהיא ``מהו המקביל המרחבי למסנן בעל התגובה האינסופית?``, שכן בהקשר של מערכי חיישנים, חיסכון במשאבים מתבטא בהוזלה משמעותית ומאפשר את מזעור המערכת.

המחקר בוצע בהנחייתם של פרופ' ישראל כהן בפקולטה להנדסת חשמל ומחשבים ודר' צבי דבורקינד מחברת רפאל.

Itay Yehezkel Karo, Tsvi Gregory Dvorkind, and Israel Cohen. Source localization with feedback beamforming. IEEE Transactions on Signal Processing, 69:631–640, 2021.

תודות

בראש ובראשונה, תודתי נתונה לאשתי הדס על שנתנה לי את הזמן, המקום והתמיכה האינסופית לסיים את עבודה זו למרות כל הקשיים והסגרים שחווינו בעקבות התפרצות נגיף הקורונה. הערכתי העמוקה נתונה גם להורי על שעודדו אותי לשאוף גבוה ולהשיג את מטרותי.

ברצוני גם להודות לדר' צבי דבורקינד על ההדרכה הבלתי מתפשרת וההכוונה אל עבר שאילת השאלות הנכונות מבלי לפספס אף פרט, עקרונות שהוכיחו עצמם מעל ומעבר בכך שהמאמר כמעט והתקבל בהגשה הראשונה.

תודה מיוחדת נתונה לפרופ' ישראל כהן על ההכוונה והליווי תוך מתן דגשים מכריעים, בנוסף על שיתוף ידיעותיו ונסיונו הרבים.

אני מודה לטכניון על התמיכה הכספית הנדיבה בהשתלמותי.

איכון מקור על ידי עיצוב אלומה עם משוב

חיבור על מחקר

לשם מילוי חלקי של הדרישות לקבלת התואר
מגיסטר למדעים בהנדסת חשמל

איתי יחזקאל קארו

הוגש לסנט הטכניון — מכון טכנולוגי לישראל
תמוז התשפ"א חיפה יוני 2021

איכון מקור על ידי עיצוב אלומה עם משוב

איתי יחזקאל קארו